https://doi.org/10.5194/egusphere-2024-3692
Preprint. Discussion started: 21 January 2025
© Author(s) 2025. CC BY 4.0 License.

pyVPRM: A next-generation Vegetation Photosynthesis and Respiration Model for the post-MODIS era

Theo Glauch[1,2], Julia Marshall[1], Christoph Gerbig[3], Santiago Botía[3], Michał Gałkowski[3,4], Sanam N. Vardag[2,5], and André Butz[2,5]

[1]Deutsches Zentrum für Luft- und Raumfahrt, Institut für Physik der Atmosphäre, Oberpfaffenhofen, Germany
[2]Heidelberg University, Institute of Environmental Physics, Heidelberg, Germany
[3]Max Planck Institute for Biogeochemistry, Jena, Germany
[4]AGH University of Kraków, Kraków, Poland
[5]Heidelberg University, Heidelberg Center for the Environment

Correspondence: Theo Glauch (theo.glauch@dlr.de)

Abstract. The Vegetation Photosynthesis and Respiration Model (VPRM) is a well-established tool to estimate carbon exchange fluxes between the atmosphere and the biosphere. The gross primary production (GPP) and respiration (R_{eco}) of the ecosystem are modelled separately at high spatial and temporal resolution using the satellite-derived Enhanced Vegetation Index (EVI) and Land Surface Water Index (LSWI), as well as meteorological variables for solar irradiance and surface temperature. The net ecosystem exchange (NEE) is calculated as the difference between the gross fluxes GPP and Respiration. VPRM is widely used as a biospheric flux model in atmospheric transport modeling, most often on scales ranging from city to continent, but also in studies of biospheric carbon budgets and their changes with climate extremes. Historically, satellite-based surface reflectances from the 500-m-resolution Moderate Resolution Imaging Spectroradiometer (MODIS) have been used to determine the EVI and LSWI. However, MODIS is reaching the end of its lifetime and will soon be decommissioned. Therefore, we present an updated version of VPRM, *pyVPRM*, which provides a software framework with a modular structure that can be used with various satellite products, land cover maps, meteorological data sources, and VPRM model parameterizations. Our tool naturally provides an interface to use satellite data from Sentinel-2, MODIS and VIIRS, as well as global high-resolution land cover classification maps from the Copernicus Dynamic Land Cover Collection 3 and ESA World Cover at 100 m and 10 m resolution, respectively. Neither product is static, hence dynamic changes of the land cover from year to year can be represented. Using Sentinel-2, ecosystem fluxes can be calculated at a resolution of up to 20 m, providing more accurate flux estimates in heterogeneous landscapes like croplands and allowing to resolve small-scale vegetation patches as common in urban areas. In contrast, VIIRS data are at the same resolution as MODIS, and thus provide for continuity once MODIS is discontinued, requiring only minor adjustments to the VPRM data preprocessing. In addition, *pyVPRM* improves the data handling, for example for snow-covered scenes. This paper presents the *pyVPRM* framework, discusses changes and improvements compared to previous VPRM implementations, and provides VPRM parameters for the European domain based on indices calculated from MODIS, Sentinel-2 and VIIRS using a new, wind-speed-optimized selection of eddy-covariance observations from 97 flux tower sites. Using *pyVPRM* and the new parameters we observe significant improvements in the estimation of the European carbon budget. The results are well conform with those from inversion studies.

https://doi.org/10.5194/egusphere-2024-3692
Preprint. Discussion started: 21 January 2025
© Author(s) 2025. CC BY 4.0 License.

1 Introduction

Carbon dioxide (CO_2) is the most important anthropogenically-influenced greenhouse gas in the Earth's atmosphere and plays a decisive role in the carbon cycle. Carbon cycles between the different compartments/reservoirs (i.e. atmosphere, oceans, biosphere, etc.) of the Earth system on different time scales. The largest exchange flux of carbon is between the atmosphere and the terrestrial biosphere (Friedlingstein et al., 2023). This uptake flux is driven by the biosphere's photosynthesis (GPP), the conversion of carbon dioxide, light and water into sugar and oxygen. At the same time, carbon dioxide is released back to the atmosphere by respiration from plants and soil. The net vegetation flux into the atmosphere, the net ecosystem exchange (NEE), is given by the difference between GPP and respiration. With a yearly global GPP of around 120 GtC, biospheric carbon dioxide fluxes are about an order of magnitude larger than anthropogenic emissions (with yearly emission of 11.1 GtC in 2022; see Friedlingstein et al., 2023). Clearly, biospheric fluxes have an important impact on the observed CO_2 concentrations in the atmosphere.

Terrestrial Biosphere Models (TBMs) are commonly used to simulate the carbon exchange between the biosphere and the atmosphere. They can be used to study the carbon budget of the terrestrial biosphere, as well as the impact of droughts and other climate extremes (Thompson et al., 2020; Stocker et al., 2019). Frequently, TBM outputs are also used as an input in atmospheric transport models, e.g. for the (inverse or top-down) estimation of carbon budgets from anthropogenic and natural sources from city- to global scale (Bousquet et al., 1999; Sargent et al., 2018). Those top-down estimates of anthropogenic CO_2 emissions, informed by atmospheric concentration measurements, are expected to become an integral part of the global stocktakes required by international climate treaties (Maksyutov et al., 2019). They provide complementary information to the "bottom-up" methods, which combine activity data with emission factors to derive the budget.

The Vegetation Photosynthesis and Respiration Model (VPRM) is a well-established light-use-efficiency terrestrial biosphere model that estimates GPP, NEE and respiration from satellite-derived indices and meteorological drivers (Mahadevan et al., 2008). VPRM parameters are estimated using in-situ measurements from eddy-covariance flux towers in different regions, different years and across different vegetation classes. Historically, VPRM was mainly used with observations from the 500-m-resolution MODIS instrument (Moderate Resolution Imaging Spectroradiometer), installed aboard the Terra and Aqua satellites[1] combined with the 1-km-resolution SYNMAP land cover classification map (Jung et al., 2006). The first MODIS sensor was launched in 1999 and since then the series of instruments have provided nearly a quarter-century time series of consistent data with high temporal resolution. Due to onboard fuel shortage MODIS will be decommissioned at the end of 2025, and hence alternative data sources are needed for VPRM. In this paper, we present a new software package – *pyVPRM*[2] – which adapts the VPRM to the post-MODIS era. It has an interface for new satellite data sets (Sentinel-2, VIIRS) and high-resolution land cover products (Copernicus Dynamic Land Cover Collection 3 (Buchhorn et al., 2020), ESA WorldCover

[1] MODIS bands 1 and 2 have a 250 m resolution. Throughout this paper we define the VPRM model resolution as the lowest resolution among all the required bands.

[2] https://github.com/tglauch/pyVPRM

https://doi.org/10.5194/egusphere-2024-3692
Preprint. Discussion started: 21 January 2025
© Author(s) 2025. CC BY 4.0 License.

(Zanaga et al., 2022), and MapBiomas (Souza et al., 2020)). Furthermore, it provides several improvements in terms of data handling, including the treatment of snow-covered scenes to improve stability and the use of the actual measurement time from the 8-day MODIS product when smoothing the data. This allows for a more accurate estimation of biospheric carbon dioxide fluxes, especially in regions with highly heterogeneous landscapes like cities or croplands.

Thanks to its modular structure, *pyVPRM* can be easily extended to use further satellite products, land cover maps, meteorological data sets, and VRPM model parameterizations. Different approaches have been used in the literature, aiming to have a more sophisticated term for R_{eco} by, for example, including additional information on water stress (Gourdji et al., 2022) or adjusting the temperature response function (Sun et al., 2023). Other customized VPRM applications are the UrbanVPRM model for cities (Hardiman et al., 2017), the PolarVPRM for high-latitude ecosystems (Luus and Lin, 2015), a regional version for China (China-VPRM Dayalu et al., 2018), approaches that incorporate information from solar-induced fluorescence (Commane et al., 2017) and a version to run online in the greenhouse gas module of the Weather Research and Forecasting Model (WRF, Ahmadov et al., 2009).

This paper is structured as follows: In Sect. 2 we review the methodology of the standard VPRM model (Mahadevan et al., 2008), in Sect. 3 we discuss the improvements and changes in *pyVPRM*, in Sect. 4 we describe the estimation of the VPRM parameters for MODIS, VIIRS and Sentinel-2 using a new selection of European flux tower sites, in Sect. 5 we discuss those parameters and their implications for European biospheric fluxes, in Sect. 6 we provide a discussion on the improvements, and conclude in section Sect. 7 with a summary and outlook. A brief overview of the code structure is provided in Appendix A.

2 Review of the VPRM model

It should be noted that VPRM is not a centrally managed model, and implementations present throughout the literature differ significantly in their choices of vegetation classes and model equations. The following discussion focuses on the original VPRM model implementation (Mahadevan et al., 2008) (called the *vprm_base* module in *pyVPRM*).

In our example for the European domain, we use eight vegetation classes: evergreen forest, deciduous forest, mixed forest, shrubland, cropland, grassland, urban/non-vegetated areas and wetland. In contrast to previously published datasets (e.g. Gerbig and Koch, 2021), we have dropped the class 'savanna' as it is a mix of grassland and woodland which can be well separated with modern, high-resolution land cover products. Moreover it does not play a major role in Europe. On the other hand, we have added a 'wetland' class as many new flux tower sites covering this land cover category have become available in Europe.

All VPRM model implementations split the CO_2 flux between the terrestrial biosphere and atmosphere into two parts: Gross Primary Production driven by photosynthesis, and the sum of soil and plant respiration. In the standard VPRM (Mahadevan et al., 2008), the GPP is parameterized as

$$\mathrm{GPP} = \epsilon \times \frac{1}{1+\mathrm{PAR}/\mathrm{PAR}_0} \times \mathrm{PAR} \times \mathrm{EVI}. \tag{1}$$

Here, EVI is the remote-sensing-based Enhanced Vegetation Index (EVI), which is closely related to the productivity of vegetation (Huete et al., 2002). It is used as a measure for the fraction of absorbed photosynthetically-active radiation (fAPAR,

https://doi.org/10.5194/egusphere-2024-3692
Preprint. Discussion started: 21 January 2025
© Author(s) 2025. CC BY 4.0 License.

at wavelengths between around $400-700\,\mathrm{nm}$) available for photosynthesis. EVI is usually based on measurements in the red, near-infrared and blue bands, but a variant of this index can be calculated using only the red and infrared bands (see Sect. 3.1.1 for details). In contrast to other vegetation indices, like the Normalized Difference Vegetation Index (NDVI, Rouse et al., 1974), it is more sensitive to variations in canopy structure, including leaf area index (LAI), canopy type and plant physiognomy (Huete et al., 2002). The negative sign of the GPP indicates a carbon uptake, i.e. flux from the atmosphere to the biosphere.

The total amount of incoming photosynthetically-active radiation can be approximated through the incoming shortwave (SW) radiation (direct and diffuse) at the surface, using the relationship PAR $\approx 0.505/\mathrm{SW}$ (Mahadevan et al., 2008). The term 1/(1+PAR/PAR$_0$) describes the saturation of the plants' photosynthetic activity. PAR$_0$ is the half-saturation value, one of the parameters fitted in the model for each vegetation class. Finally, ϵ is the light-use efficiency, which is the product of four terms with values between 0 and 1:

$$\epsilon = \lambda \times T_{scale} \times W_{scale} \times P_{scale} \tag{2}$$

Here, T_{scale} describes the temperature dependence of the photosynthesis, defined as

$$T_{scale} = \frac{(T-T_{min})(T-T_{max})}{(T-T_{min})(T-T_{max})-(T-T_{opt})^2}, \tag{3}$$

with T_{min}, T_{opt} and T_{max} referring to literature-derived values of the minimal, optimal and maximal temperatures for photosynthesis for each vegetation class in degrees Celsius. At temperature below T_{min} or above T_{max}, photosynthetic activity is set to 0. Usually, the temperature T is given by the 2-m temperature, which is available in most meteorological models.

The variable P_{scale} accounts for the effect of leaf age and is defined separately for the different vegetation types. For evergreen forests,

$$P_{scale} = 1, \tag{4}$$

for grassland (and savannas),

$$P_{scale} = (1+\mathrm{LSWI})/2, \tag{5}$$

and for all other vegetation classes

$$P_{scale} = \begin{cases} 1, & \text{between leaf full expansion and senescence} \\ (1+\mathrm{LSWI})/2, & \text{during bud burst to leaf full expansion and during senescence.} \end{cases} \tag{6}$$

Here, LSWI is the Land Surface Water Index, which captures the effects of water stress and leaf phenology and is derived using satellite data in the near and shortwave infrared (see section 3.1.1 for details). The periods from bud burst to leaf full expansion and senescence are defined as those where the EVI is below a threshold of

$$\mathrm{TH}_{\text{leaf full expansion}} = \mathrm{EVI}_{min} + 0.55 \cdot (\mathrm{EVI}_{max} - \mathrm{EVI}_{min}) \tag{7}$$

Both the maximum and minimum EVI values (EVI_{max} and EVI_{min}) are calculated for each satellite pixel over an entire year.

https://doi.org/10.5194/egusphere-2024-3692
Preprint. Discussion started: 21 January 2025
© Author(s) 2025. CC BY 4.0 License.

The variable W_{scale} represents the canopy water content as a measure of the water stress. It is defined as

$$W_{scale} = \begin{cases} \frac{\text{LSWI}-\text{LSWI}_{min}}{\text{LSWI}_{max}-\text{LSWI}_{min}}, & \text{grassland (and savanna),} \\ \frac{1+\text{LSWI}}{1+\text{LSWI}_{max}}, & \text{all other classes.} \end{cases} \tag{8}$$

The LSWI thresholds, LSWI_{max} and LSWI_{min}, are calculated as the pixel-wise maximum/minimum LSWI during the growing season, eq. (7). Using this threshold ensures that the maximum LSWI lies within the growing season. This is important as LSWI is sensitive to snow periods.

Note that for grassland we follow the parameterization of Matross et al. (2006) which takes into account that grasslands are xeric ecosystems. This represents a deviation from the work of Mahadevan et al. (2008) relevant for eq. (5) and eq. (8).

Finally, λ is a fitting parameter that accounts for the quantum yield and also includes vegetation-class-specific (linear) corrections to the other parameters. For well-watered C3 plants, the quantum yield is expected to be around 1/6 (Mahadevan et al., 2008).

The parameterization of ecosystem respiration, R_{eco}, is a simple linear function with two free parameters, α and β.

$$\text{R}_{eco} = \alpha \times \max(T, T_{\text{low}}) + \beta. \tag{9}$$

When the $T < T_{\text{low}}$ the temperature in Eq. (9) is set to T_{low} to maintain a minimal level of respiration as the (winter) soil temperature is typically higher than the air temperature.

In summary, four free parameters α, β, PAR_0 and λ have to be fitted for each vegetation type.

3 The *pyVPRM* package

With *pyVPRM*, we provide a Python-based software package that can be used for a wide range of applications of the vegetation photosynthesis and respiration model (VPRM). It has a modular structure and can be used to combine different satellite data products, land cover maps, meteorology datasets, and VPRM model parameterizations. It provides all functions to fit VPRM parameters, produce biospheric fluxes, and generate input files for using VPRM online in mesoscale atmospheric transport models like the Weather Research and Forecasting Model (WRF-GHG (Beck et al., 2012) / WRF-Chem (Peckham, 2012)) or the ICON-ART Model (Schröter et al., 2018). An overview of the modular structure of *pyVPRM* is given in Fig. 1.

3.1 Satellite data

In general, all multi-spectral satellites that have at least a near-infrared, a short wavelength infrared and a red channel are suitable for constructing the indices required in the VPRM model. In addition, a blue band can be useful for the calculation of the enhanced vegetation index (EVI), but is not strictly necessary. While MODIS was used historically, other satellite data sets are now available as well. Notably, Sentinel-2 (ESA, 2024) improves the VPRM spatial resolution from 500 m (MODIS (Vermote, 2021), VIIRS (Vermote et al., 2023)) down to 20 m, which is especially useful for modelling ecosystem carbon dioxide fluxes in urban areas or in heterogeneous landscapes such as croplands and agricultural grasslands. The choice of the

https://doi.org/10.5194/egusphere-2024-3692
Preprint. Discussion started: 21 January 2025
© Author(s) 2025. CC BY 4.0 License.

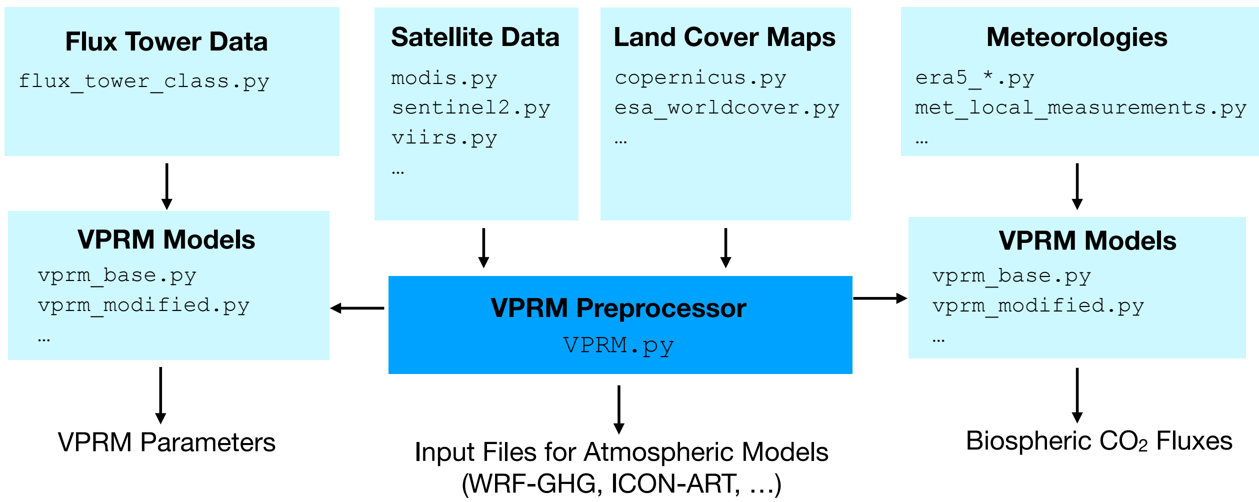

Figure 1. Modular structure of *pyVPRM*. Using different combinations of inputs one can either calculate VPRM parameters, generate VPRM input files for atmospheric models or calculate 'offline' biospheric carbon dioxide fluxes. The type of the module is shown in bold with corresponding (exemplary) file name below. This is subject to changes and extensions in the further development of the model. The VPRM preprocessor is the central class that prepares the satellite images and land cover maps as described in Sect. 3.1 to Sect. 3.3. More details are found in Appendix A.

satellite mission ultimately depends on the specific user requirements, e.g. the required spatial resolution, data availability and satellite revisit time, especially when persistent cloud cover is an issue.

pyVPRM naturally supports three satellite missions: MODIS, VIIRS, and Sentinel-2. However, the implementation of our *pyVPRM* framework allows for easy extension to other missions (like Landsat) or data fusion products of different satellite data collections (Moreno-Martínez et al., 2020). VIIRS is of particular interest as it is the drop-in replacement for MODIS after its discontinuation. A summary of the three satellite missions and the relevant mission specifications are given in Table 1. Evidently, there is a large overlap between the wavelength bands among the missions. Nevertheless, we fit a different set of VPRM parameters for each mission, accounting also for differences in the data processing, like the atmospheric correction.

The MODIS sensor is placed on two research satellites – Aqua and Terra – with afternoon and morning orbits, respectively. Hence, combining data from the two satellite missions helps to mitigate sparse observations and improve the modelling of vegetation dynamics. This is especially useful in regions with high cloud coverage like the tropics. MODIS (Terra, Aqua) and VIIRS products are available as daily observations (MOD09GA, MYD09GA, VNP09GA) and as aggregated 8-day products (MOD09A1, MYD09A1, VNP09H1). The choice of the optimal product depends on the expected vegetation dynamics and available computing resources.

https://doi.org/10.5194/egusphere-2024-3692
Preprint. Discussion started: 21 January 2025
© Author(s) 2025. CC BY 4.0 License.

Feature	MODIS (Terra, Aqua)	VIIRS (SuomiNPP)	Sentinel-2A and 2B
Red band [nm]	620–670 (Band1)	600-680 (Band I1)	664.6 ± 31 (Band 4)
Near-infrared band (NIR) [nm]	841–876 (Band 2)	846-885 (Band I2)	864.7 ±21 (Band 8A)
Shortwave infrared band (SWIR) [nm]	1628–1652 (Band 6)	1580-1640 (Band I3)	1613.7 ± 91 (Band 11)
Blue band [nm]	459–479 (Band 3)	–	492.4 ± 66 (Band 2)
Spatial Resolution	500m	500m	20m
Revisit frequency (at equator)	1-2 days	1-2days	5 days
Data availability	1999 - now	2011 - now	2015 - now
Data product	MOD09GA, MYD09GA MOD09A1, MYD09A1	VNP09GA VNP09H1	Sentinel-2 Collection 1 Level-2A

Table 1. Overview of the relevant properties of the different satellite missions. The spatial resolution is given as the minimal resolution of all bands required for the VPRM calculations. In addition, the table names the MODIS (Vermote, 2021), VIIRS (Vermote et al., 2023) and Sentinel-2 (ESA, 2024) data products used for the VPRM calculations in this paper. Further information on the MODIS and VIIRS products can be found on the website of the Land Processes Distributed Active Archive Center (LP DAAC) within the NASA Earth Observing System Data and Information System (https://lpdaac.usgs.gov/, visited 27-08-2024). Note that for Sentinel-2 there is a slight difference of the bands between Sentinel-2A and Sentinel-2B. The values given here represent the bands of Sentinel-2A.

3.1.1 Satellite indices

EVI is sensitive to the leaf area index, canopy type and plant physiognomy. It is defined using the reflectances in red (ρ_{Red}), infrared (ρ_{NIR}), and blue (ρ_{Blue}) following Huete et al. (2002) as

$$\text{EVI} = G \times \frac{(\rho_{\text{NIR}} - \rho_{\text{Red}})}{(\rho_{\text{NIR}} + C_1 \times \rho_{\text{Red}} - C_2 \times \rho_{\text{Blue}} + L)} \tag{10}$$

where, in general, the free parameters G, C_1, C_2 and L depend on the satellite sensor. For MODIS and Sentinel-2 we use $G = 2.5$, $C_1 = 6$, $C_2 = 7.5$, and $L = 1$ (Huete et al., 2002). While the detection of vegetation is governed by the red and infrared band, the blue channel was added to account for the impact of atmospheric aerosols. It is, however, also possible to define an alternate enhanced vegetation index without a blue band (Jiang et al., 2008), EVI2, as

$$\text{EVI2} = G \times \frac{(\rho_{\text{NIR}} - \rho_{\text{Red}})}{(\rho_{\text{NIR}} + C_1 \times \rho_{\text{Red}} + L)} \tag{11}$$

with only three free parameters, G,C_1 and L. In our case, we use EVI2 for data from the VIIRS satellite, as no blue band is available. Here, the free parameters are set to $G = 2.5$, $C_1 = 2.4$, and $L = 1$ (Huete et al., 2002).

In addition to EVI, VPRM uses another remote-sensing-based index – the land surface water index (LSWI) – to estimate the vegetation and soil water content. LSWI requires a near infrared and a shortwave infrared band and is calculated for all satellite missions following Gao (1995) as

$$\text{LSWI} = \frac{\rho_{\text{NIR}} - \rho_{\text{SWIR}}}{\rho_{\text{NIR}} + \rho_{\text{SWIR}}} \tag{12}$$

https://doi.org/10.5194/egusphere-2024-3692
Preprint. Discussion started: 21 January 2025
© Author(s) 2025. CC BY 4.0 License.

In *pyVPRM*, both EVI and LSWI are calculated within the VPRM preprocessor class (see Fig. 1) whenever a new satellite image is added to the instance (using the *add_sat_img(.)* function).

3.1.2 Data quality masking

Not every satellite observation is useful for the estimation of EVI and LSWI. Typical problems include cloudiness, shadows and problems in the satellite retrieval. In order to get a reliable estimate of the time evolution of the two indices, pixels that have any of the previously mentioned problems are masked out from all further calculations using the data quality flags of the respective data products. Specifically, we only use pixels that have the highest-quality data in all bands, do not show any kind of cloud cover (also cirrus) and are free from cloud shadows. Periods with snow are treated differently, see Sect. 3.1.3. Details on the data quality flags for the satellite products discussed in this paper can be found in Table B1 (for MODIS), Table B2 (for VIIRS), and Table B3 (for Sentinel-2). In *pyVPRM* the *mask_bad_pixels(.)*, *mask_bad_clouds(.)* and *mask_bad_snow(.)* functions of the respective satellite image class are used.

3.1.3 Time smoothing

We expect both LSWI and EVI to be continuous functions over the year. Hence, in order to remove statistical noise, we derive daily indices through a temporal smoothing procedure (Mahadevan et al., 2008). In a first step, all the available satellite scenes for at least a year are loaded and combined to a data cube with two spatial dimensions and a time dimension. Subsequently, the array of observations in each pixel is smoothed using a *lowess* (LOcally WEighted Scatterplot Smoothing) function (Cleveland, 1979) (using the *lowess(.)* function of the VPRM prepocessor). The smoothing takes into account the specific observation time of each scene, even if 8-day products (like MOD09A1) are being used. Finally, the fitted lowess function is evaluated for each day of the year, producing a data cube storing daily EVI and LSWI for each pixel. It is good practice to include additional satellite scenes before the beginning and after the end of the year of interest to avoid boundary effects.

While the lowess function is fairly stable against noise, instabilities may arise if the vegetation is covered by snow for several months of the year (especially at high latitudes). Hence, instead of masking out every observation with detected snow cover, as we do for clouds and other low quality observations, during snow-covered periods we set the EVI and LSWI to the minimum value observed outside of the snow-covered period. This stabilizes the numerical fit and does not impact the estimated carbon fluxes, as the temperature during snow-covered periods is usually below 0°C, resulting in negligible GPP (see Eq. (3)). The respiration, on the other hand, is independent of the satellite indices.

Figure 2 shows an example of the lowess-filtered values for EVI and LSWI from MODIS and Sentinel-2 at the German cropland flux tower site Selhausen Juelich (DE-RuS; 50.8659°N, 6.4471°E) in 2022. For comparison, hourly measured GPP is shown in the background. The typical footprint extension at the eddy covariance site DE-RuS is around 50 m (Kormann and Meixner, 2001). Hence, the poor agreement of the MODIS EVI curve with the measured GPP is a direct result of the limited spatial resolution of MODIS in such a heterogeneous landscape. In fact, the observed seasonal cycle of the satellite indices is a superposition of the seasonal cycles of the fields contained within the MODIS pixel (white). In contrast, the Sentinel-2 indices more closely follow the seasonal cycle of the GPP measurements. Uncertainties in Sentinel-2 arise mainly through the

https://doi.org/10.5194/egusphere-2024-3692
Preprint. Discussion started: 21 January 2025
© Author(s) 2025. CC BY 4.0 License.

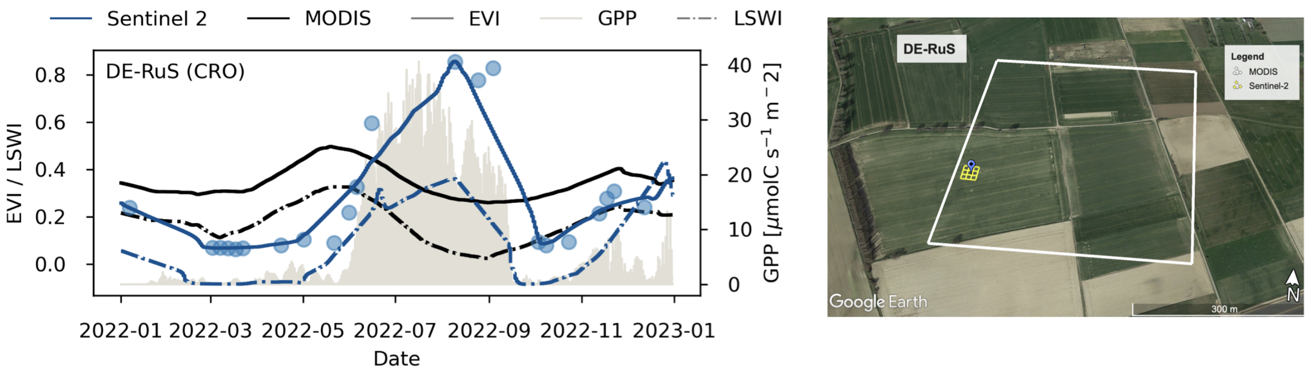

Figure 2. Left: Comparison of the hourly GPP at the cropland flux tower site Selhausen Juelich (DE-RuS; 50.8659°N, 6.4471°E) with the satellite indices (EVI, LSWI) for Sentinel-2 and MODIS over the year 2022. GPP (in light grey) is based on the ICOS daytime partitioning method. The solid and dash-dotted lines show the lowess-smoothed LSWI and EVI, respectively. Values from MODIS are shown in black, while values for Sentinel-2 are shown in blue. The blue points show the unfiltered EVI measurements for the case of Sentinel-2. Right: Satellite image of the site with the relevant MODIS (white) and Sentinel-2 pixels (yellow) overlaid. The position of the flux tower is shown with a blue pin. Map data ©2024 Google.

limited revisit frequency. While MODIS provides one image every 1-2 days under clear-sky conditions, Sentinel-2 takes only one image every $\sim$5 days. Hence, in time periods with frequent cloud coverage, observations can become sparse. The resulting interpolation errors are largest in periods of strong leaf phenological change.

3.2 Land cover classification

The standard VPRM model (Mahadevan et al., 2008) is fitted with four independent parameters for each vegetation class. In addition to remote sensing data, the estimation of terrestrial carbon fluxes with VPRM therefore requires a land cover classification map that covers the entire area of interest. By default the *pyVPRM* package provides interfaces for the global 100-m Copernicus Dynamic Land Cover Collection 3 (Buchhorn et al., 2020) and the global 10-m ESA WorldCover (Zanaga et al., 2022) product. Neither product is static in that they provide different maps for different years to account for land use changes. Table 2 shows the mapping between the land cover types for the two products and the eight VPRM classes used in this paper. Note that ESA WorldCover has only one forest class and, therefore, contains no information on the forest type. Hence, it is rational to generate a hybrid product that uses ESA WorldCover as a baseline, but replaces the forest sub-class information with that of the (lower-resolution) Copernicus Dynamic Land Cover Collection 3 (Buchhorn et al., 2020). A sequence of land cover maps with increasing resolution is shown for a region around Vienna in Fig. 3. Note that while SYNMAP (Jung et al., 2006) does not resolve much of the structure inside the built-up urban area, the Copernicus Dynamic Land Cover Collection 3 (Buchhorn et al., 2020) product and especially the hybrid product can resolve vegetated areas within the built-up area and heterogeneity within the forested area to the west of the city and the surrounding croplands.

© Author(s) 2025. CC BY 4.0 License.

	Copernicus Dynamic Land Cover Collection 3	ESA WorldCover
Evergreen Forest	111, 112, 121, 122	10^*
Deciduous Forest	113, 114, 123, 124	10^*
Mixed Forest	115, 126, 116, 125	10^*
Shrubland	20	20
Cropland	40	40
Grassland	30, 100	30, 100
Non-Vegetated	50, 60, 70, 80, 200	50, 60, 70, 80
Wetland	90	90, 95

Table 2. Mapping from land cover classifications in the Copernicus Dynamic Land Cover Collection 3 (Buchhorn et al., 2020) and ESA WorldCover (Zanaga et al., 2022) to the eight VPRM classes used in this paper. Note (*) that the ESA WorldCover has only one forest class. Hence it is advised to use a hybrid of the two products in this table, using the forest-type classification of the 100-m products of the Copernicus Dynamic Land Cover Collection 3. *pyVPRM* uses YAML configuration files to define the mapping and auxiliary data for the vegetation classes.

In many cases the land cover maps will not have the same coordinate reference system and resolution as the satellite data products. Hence, the land cover map needs to be regridded to match the satellite data. *pyVPRM* uses the xESMF package (Zhuang et al., 2023) which is based on the Earth System Modelling Framework (ESMF) (Hill et al., 2004). xESMF supports general curvilinear grids and different regridding algorithms, most importantly bilinear and conservative, which is designed to preserve total quantities. Using conservative regridding, the *add_land_cover_map(.)* function of *pyVPRM*'s VPRM preprocessor calculates the fraction of each land cover class from the input (land cover) grid for each pixel in the destination (satellite) grid. The result is a 2-d vegetation fraction map for each vegetation class with the same spatial extent and on the same grid as the satellite scenes.

3.3 VPRM data preparation and calculation of carbon fluxes

In order to generate the VPRM fluxes for a given region we use Eq. (1) and Eq. (9) in matrix form. This requires the meteorological data (e.g. temperature and solar irradiance) and the land cover information to be regridded onto the native satellite grid using the *xESMF* package, see Sect. 3.2. With all the data on the same grid, the net ecosystem exchange (or GPP and respiration) for each land cover type is calculated by matrix multiplication (using the *make_vprm_predictions(.)* function of the VPRM model class). Summing up all land cover types with their respective fractional weight, F_v, gives the total flux per pixel, i.e.

$$\mathrm{NEE_{2D}} = \sum_{\substack{v\in \\ \text{veg classes}}} F_v \times \left[-(\lambda_v \times T_{scale,v} \times W_{scale} \times P_{scale,v}) \times \frac{1}{1+\mathrm{PAR}/\mathrm{PAR}_{0,v}} \times \mathrm{PAR} \times \mathrm{EVI} + \alpha_v \times \max(T, T_{\mathrm{low},v}) + b_v \right] \tag{13}$$

https://doi.org/10.5194/egusphere-2024-3692
Preprint. Discussion started: 21 January 2025
© Author(s) 2025. CC BY 4.0 License.

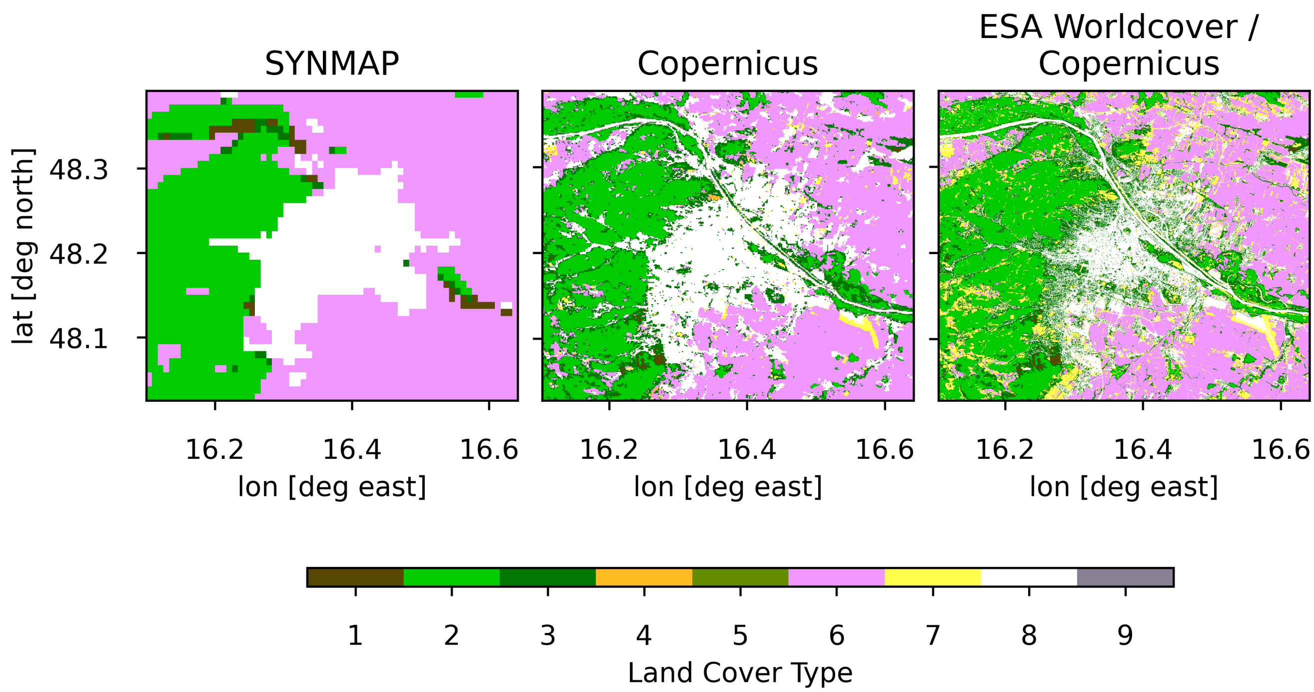

Figure 3. The region around Vienna for three different land cover classification products: SYNMAP (left), the 100-m product of the Copernicus Dynamic Land Cover Collection 3 (middle), and a hybrid between ESA Worldcover and the Copernicus Dynamic Land Cover Collection 3 (right). Different colors (numbers) represent the different vegetation classes in our VPRM model for Europe: Evergreen (1), deciduous forest (2), mixed forest (3), shrubland (4), cropland (6), grassland (7), non-vegetated area (8), wetland (9). The class savanna (5) is not used in this implementation, but remains in the numbered list for legacy reasons.

As an example, we have calculated the hourly NEE in the 19 km x 19 km region around Vienna using a combination of Sentinel-2 data for 2022, a hybrid land cover map as explained above and the ERA5-Land meteorological re-analysis data from the European Centre for Medium-Range Weather Forecasts (ECMWF) (Hersbach et al., 2020) [3]. The monthly aggregated results for May, July and October are shown in Fig.4.

3.4 VPRM preprocessor for online flux calculation in mesoscale atmospheric transport models

Complementary to the direct calculation of carbon fluxes, *pyVPRM* can also be used as a preprocessor to generate input files for online flux calculation within mesoscale atmospheric models, such as the greenhouse gas module of the Weather Research and Forecasting (WRF-GHG/WRF-Chem) Model or ICON-ART. In this case, the fluxes are calculated using the 2-m temperature and shortwave radiation at the surface calculated within the forecast model. The procedure for the generation of the input files

[3] For shortwave radiation we use the parameter surface_solar_radiation_downwards (paramID:169) and for the 2m-temperature the parameter 2m_temperature (paramID:167). See https://confluence.ecmwf.int/display/CKB/ERA5 for details (viewed on 2023-08-26).

https://doi.org/10.5194/egusphere-2024-3692
Preprint. Discussion started: 21 January 2025
© Author(s) 2025. CC BY 4.0 License.

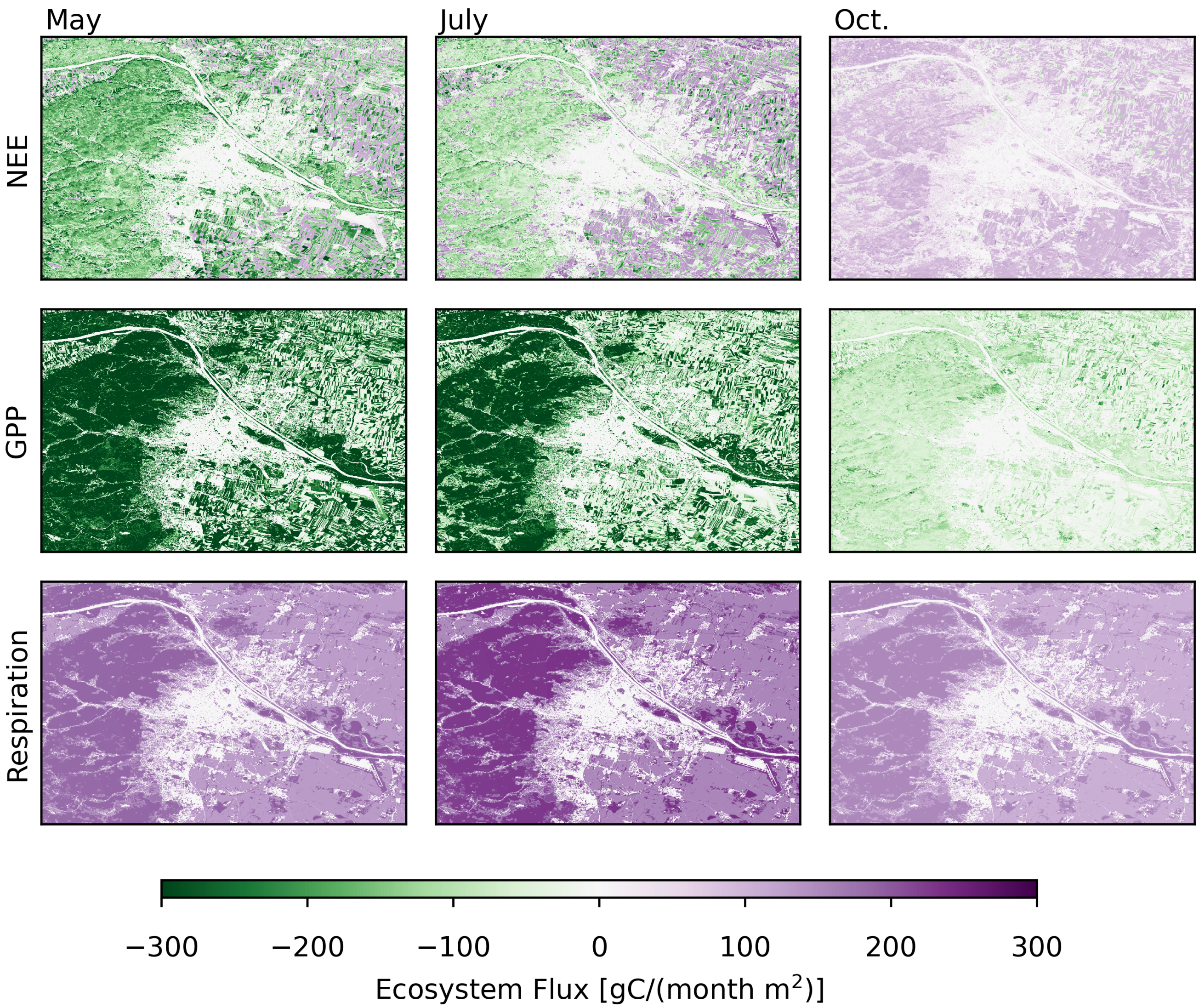

Figure 4. Monthly aggregated ecosystem fluxes for three month in the region around Vienna. The different months (May, July, October) are shown in the panels from left to right. From top to bottom net ecosystem exchange (NEE), gross primary production (GPP) and respiration are shown. Negative values represent a carbon uptake, positive fluxes show a carbon release into the atmosphere. The fluxes are based on Sentinel-2 images, a hybrid land cover map and hourly ERA5-Land meteorological data. The corresponding land cover map is shown in Fig. 3.

https://doi.org/10.5194/egusphere-2024-3692
Preprint. Discussion started: 21 January 2025
© Author(s) 2025. CC BY 4.0 License.

is similar to the procedure described in section 3.3. The difference is that, instead of using Eq. (13) to calculate the CO_2 fluxes, the EVI and LSWI fields as well as the land cover map are regridded to match the input format of the atmospheric model. Overall, the VPRM preprocessor needs to create seven files: two containing the daily EVI and LSWI for each vegetation class, four with the annual minimum and maximum EVI and LSWI for each vegetation class, and one with the pixel-wise fraction of each vegetation class. In *pyVPRM* the output files can be directly written from a VPRM preprocessor instance using the *to_wrf_output(.)* method. Figure 5 shows an example of the vegetation fractions for Europe using the Copernicus Dynamic Land Cover Collection 3 (Buchhorn et al., 2020) as input.

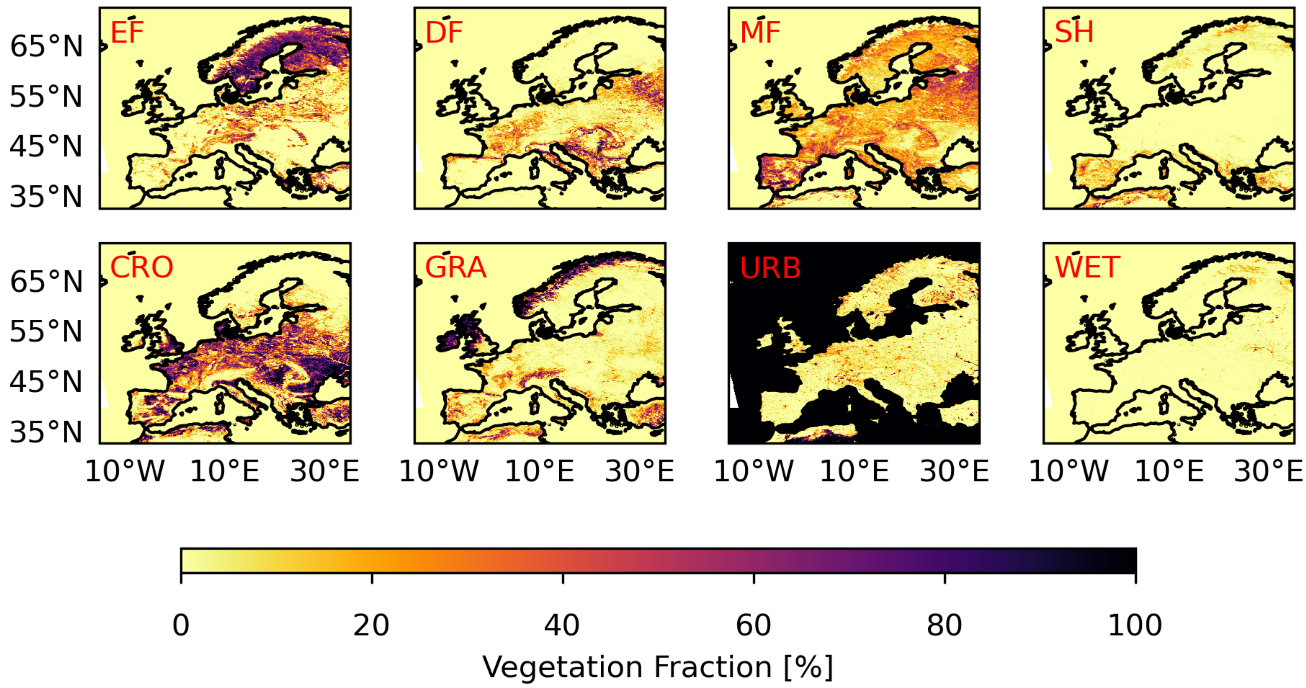

Figure 5. Vegetation fractions of the eight land cover classes used in our VPRM model, based on the Copernicus Dynamic Land Cover Collection 3. The data are regridded on a 0.25° x 0.25° regular grid. This is a typical example of a vegetation fraction map that can also be used in mesoscale atmospheric models like WRF-GHG/WRF-Chem or ICON-ART. The abbreviations are evergreen forest (EF), deciduous forest (DF), mixed forest (MF), shrubland (SH), cropland (CRO), grassland (GRA), non-vegetated (URB), and wetland (WET). Not shown here are the other files generated by the *pyVPRM* preprocessor, i.e. the EVI and LSWI maps.

4 Estimating VPRM parameters for Sentinel-2, MODIS and VIIRS

The full equation of the VPRM model, Eq. (13), contains four free parameters for each vegetation class: the quantum efficiency λ, the half saturation value of the photosynthetic activity PAR_0, and two parameters, α and β, describing the linear behavior of

https://doi.org/10.5194/egusphere-2024-3692
Preprint. Discussion started: 21 January 2025
© Author(s) 2025. CC BY 4.0 License.

the respiration with temperature. Those parameters are required to calculate the carbon fluxes, whether VPRM is used offline or within the weather prediction/tracer transport model. To estimate those parameters, in-situ CO_2 flux measurements from eddy-covariance towers are used. We show here an example of the fitting procedure for the European domain and provide an updated VPRM parameter set for Sentinel-2, MODIS and VIIRS.

4.1 Flux tower selection

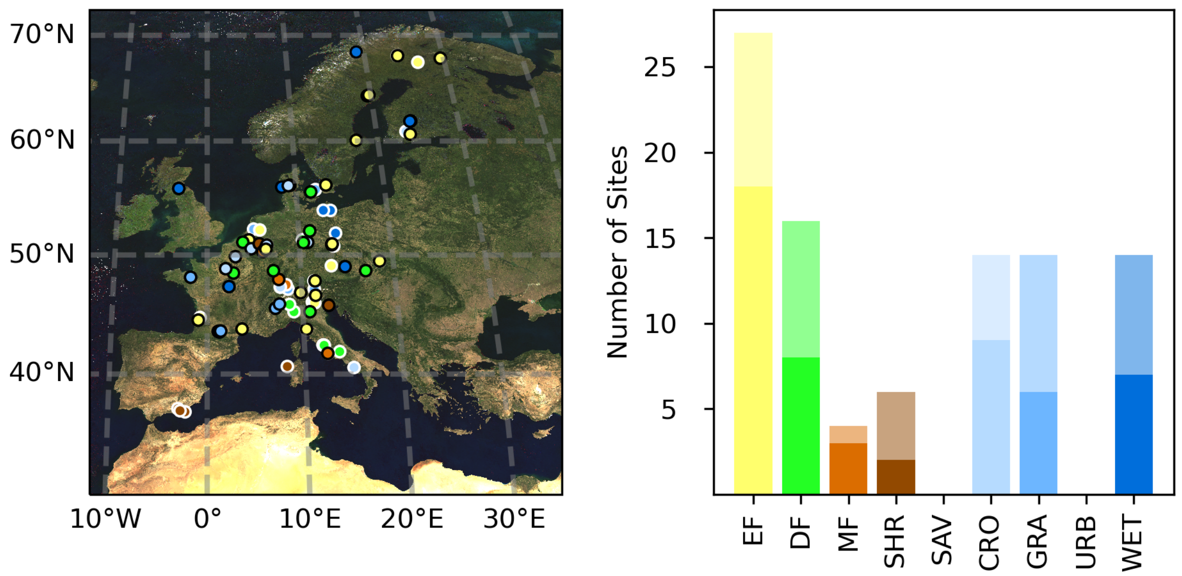

Figure 6. Left: The flux tower sites used to estimate the VPRM parameters. Circles with black and white contours indicate data that were used from the ICOS or FLUXNET data collection, respectively. Different colors show the different vegetation types with the number of sites shown in the histogram on the right. Brighter bars show the number of ICOS and FLUXNET stations with available data during the period covered by MODIS. Darker bars show the number of stations available since the launch of Sentinel-2. Abbreviations are as follows: EF - evergreen forest, DF - deciduous forest, MF - mixed forest, SHR - shrubland, CRO - cropland, GRA - grassland, WET - wetland, SAV-Savanna. Background satellite image created using MODIS data.

Several data collections provide harmonized eddy-covariance flux tower measurements for a collection of measurement sites. For example, FLUXNET (Pastorello et al., 2020) provides global data for a total of 212 sites, but only up to the year 2015. On a continental level, AmeriFlux provides data for North and South America, the ICOS Carbon portal (ICOS RI et al., 2023) provides data for Europe, and OzFlux provides data for Australia and New Zealand.

For our European application we combine data from FLUXNET and ICOS covering the period between 2002 and 2022. An overview of the locations and ecosystem types of the various stations is given in Fig. 6. For the fit of the Sentinel-2 parameters, only sites with data after 2015 can be used. Overall we use 97 sites for MODIS, 52 sites for Sentinel-2 and 68 sites for VIIRS. An overview of the stations used for parameter estimation are shown in section C for each satellite mission, respectively.

https://doi.org/10.5194/egusphere-2024-3692
Preprint. Discussion started: 21 January 2025
© Author(s) 2025. CC BY 4.0 License.

All flux towers use the eddy-covariance technique, which statistically determines vertical fluxes from turbulence (eddies) in the wind field. Flux towers therefore measure a weighted average of fluxes in the upwind direction. The spatial area from which fluxes contribute to the measurement is called the footprint, and this depends strongly on the wind speed and the height above canopy of the flux tower itself, as well as other aerodynamic quantities such as the surface roughness (Chen et al., 2009; Schmid, 1994). Optimally, the flux tower should be surrounded by a sufficiently homogeneous landscape to be representative for a specific land cover class. This is, however, not always the case. For some sites the measurement might see signals from different land cover types at different times (Järvi et al., 2012). Other sites might be located in a satellite pixel that overlaps with different land covers, see Fig. 2. For this reason, we visually inspect all sites using Google Earth and remove those that are extremely heterogeneous on the spatial scale of the satellite resolution.

4.2 Spatial smoothing

Spatial smoothing is a way to account for footprints that exceed the size of a single satellite pixel. In previous VPRM versions (Mahadevan et al., 2008), the EVI and LSWI of the nine MODIS pixels surrounding the tower location have been averaged for comparison with the flux tower data. This means averaging over a region of around $(1.5 \times 1.5)\,\mathrm{km}^2$. In many cases the averaging is therefore done over heterogeneous land cover types, leading to inconsistencies between measured and modeled fluxes, see Fig. 9.

In our case, we mitigate this problem by prioritizing time periods with relatively low wind speed and hence small tower footprints for each site. As a consequence we do not use any spatial smoothing for MODIS and VIIRS (with 500 m resolution), i.e. we only use the pixel in which the tower is located. For Sentinel-2, with a pixel size of 20 m, we use a 3 x 3 pixel (60 m x 60 m) spatial smoothing centered at the tower location.

In general, *pyVPRM* also provides the option of using arbitrary weighting kernels in the *smearing(.)* function of the VPRM preprocessor to better match the satellite observation to flux tower footprint models.

4.3 Fitting VPRM parameters

For the fit we choose only the highest quality data points, thus removing low turbulence conditions with bad flux measurements (i.e. only using data where *'NEE_VUT_REF_QC'* is 0). Further, we ensure that the data are distributed uniformly over the year and the time of the day. To do that, we group the data in two dimensions by week of the year and time of the day in three-hourly time steps. Subsequently we sample three measurements from each group, prioritizing low wind speed data points through a weighting function scaling inversely with wind speed. This leads to a selection of $\mathcal{O}(10^3)$ data points with uniform distribution over the year for each tower. The selected data are fitted using a two-step mean-squared-error fitting. In a first step, the respiration parameters are fitted for nighttime data only, thus naturally removing the light-dependent photosynthesis. In a second step, NEE is fitted using the best-fit parameters of the first step for the respiration parameters. This fitting procedure hence does not require a partitioning of the measured NEE into GPP and respiration, but rather uses the flux measurements directly. This avoids typical assumptions and uncertainties that arise when partitioning the carbon fluxes from eddy-covariance towers (Wutzler et al., 2018). In *pyVPRM* each VPRM model class has a function *fit_vprm_data(.)* that performs the fit.

https://doi.org/10.5194/egusphere-2024-3692
Preprint. Discussion started: 21 January 2025
© Author(s) 2025. CC BY 4.0 License.

5 Results

VPRM parameters for the different satellite missions (MODIS, VIIRS, Sentinel-2) for the European domain are shown in Table 3. We observe that, although the wavelength bands of MODIS and Sentinel-2 largely overlap, there are some differences between the parameters for the two products. This could be related to slight differences in the satellite bands and data collection or in the different spatio-temporal resolution of the observations. This question will be investigated in further studies. The parameters for VIIRS are calculated using EVI2 (without the blue band) and hence are not expected to be directly comparable.

	Temperatures				MODIS				Sentinel-2				VIIRS			
	T_{min}	T_{opt}	T_{max}	T_{low}	λ	par_0	α	β	λ	par_0	α	β	λ	par_0	α	β
EF	-4	15	38	-3	0.13	521.9	0.21	1.15	0.13	505.9	0.24	1.29	0.14	482.4	0.24	1.14
DF	1	21	37	0	0.13	500.8	0.23	1.26	0.11	443.1	0.26	1.37	0.13	469.7	0.28	1.11
MF	-1	18	38	0	0.14	451.1	0.19	0.93	0.14	389.8	0.18	1.44	0.15	423.8	0.19	1.20
SHR	-1	19	44	2	0.1	444.1	0.08	0.56	0.27	217.2	0.14	1.06	0.08	575.3	0.15	0.37
CRO	-3	16	50	-3	0.09	960.8	0.17	1.14	0.07	970.2	0.16	1.24	0.08	980.3	0.17	1.22
GRA	-2	17	36	-2	0.22	443.4	0.27	1.63	0.16	593.5	0.24	1.59	0.21	504.0	0.25	1.55
WET	-2	26	40	0	0.12	399.7	0.3	-0.39	0.13	322.5	0.34	-0.45	0.1	532.5	0.34	-0.58

Table 3. Overview of the VPRM parameter sets for MODIS, Sentinel-2 and VIIRS and the different ecosystems. Abbreviations are as follows: EF - evergreen forest, DF - deciduous forest, MF - mixed forest, SHR - shrubland, CRO - cropland, GRA - grassland, WET - wetland. The parameters of Gerbig (2024) can be found in Table F1 for comparison.

In order to evaluate how the high-resolution of Sentinel-2 can improve flux estimates we have studied some of the (heterogeneous) cropland flux sites in more detail. In Fig. 7 the monthly average diurnal cycle is shown for the site Selhausen Juelich (DE-RuS; 50.8659°N, 6.4471°E). Evidently, the monthly median diurnal cycle of Sentinel-2 matches the observation much better than the one from MODIS in most months. This is a direct consequence of the different seasonal cycles of the EVI, shown in Fig. 2. While the higher resolution of the Sentinel-2 images allows the growing periods of the specific field to be resolved, MODIS is averaging over several fields, resulting in a superposition of their seasonal cycles. This results in predicted fluxes in April and May that are much larger than what is observed at the site. Overall the mean-squared deviation from the measurement reduces from 43.9 (MODIS) to 7.1 (Sentinel-2). Similar effects can be observed for many cropland sites, which is especially problematic in Europe, where 38% of the land surface is covered with cropland. Fig. 8 gives an overview on the mean-squared deviation from the measurement for the cropland sites with data availability during the Sentinel-2 mission. For comparison we also show similar results for evergreen forest sites, which are usually pretty homogeneous. As expected, the majority of cropland sites show a significant reduction in the mean-square deviation while there is no trend for evergreen forests (as for the other forest classes). The full diurnal cycle of all cropland sites in Fig. 8 are shown in the appendix D. Our findings are in line with a recent study of (Bazzi et al., 2024) that found that using Sentinel-2 data significantly improves the simulation of cropland carbon dioxide fluxes in Europe.

https://doi.org/10.5194/egusphere-2024-3692
Preprint. Discussion started: 21 January 2025
© Author(s) 2025. CC BY 4.0 License.

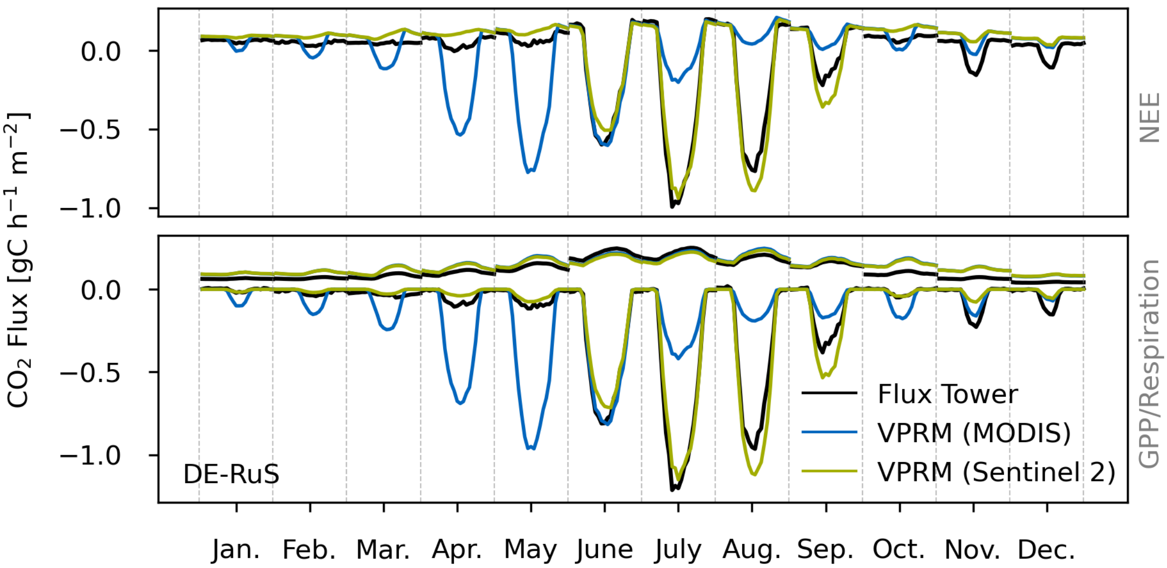

Figure 7. The mean diurnal cycle for each month at the cropland site Selhausen Juelich (DE-RuS, 50.8659°N; 6.4471°E) in 2022. The median tower measurements for each hour of the day are shown as black lines. Colored solid lines indicate the results from the VPRM model using indices from Sentinel-2 (green) and MODIS (blue). In the top panel NEE is shown and in the bottom panel GPP (negative values, carbon uptake) and respiration (positive values, carbon release) are shown. The flux partitioning is based on the night-time partitioning method with variable u* threshold (Reichstein et al., 2005).

Finally, we have compared the MODIS-based European fluxes from *pyVPRM* against those published on the ICOS Carbon Portal for the year 2023 (Gerbig and Koch, 2024), see Fig. 11. A summary of the model properties for the different flux data sets is shown in Table 4. The plot on the left shows the annual net carbon flux as published on the ICOS Carbon Portal using the old software and old model settings. The middle panel shows a model run with the same VPRM parameters and the same land cover maps as the old version but using the *pyVPRM* to run the computations. The comparison shows that the old and new software frameworks produce numerically compatible results. The right panel shows the annual fluxes using *pyVPRM* and the new VPRM parameters as well as the new land cover map. This clearly shows how the fluxes change with the new approach.

6 Discussion

Evidently, fluxes change significantly with the new VPRM version. This is primarily driven by improvements in the VPRM parameter estimation for cropland and grassland. The origin of those improvements is illustrated in Fig. 9. Two changes are important here: one related to the spatial smoothing of the satellite data, and one relating to the fit procedure itself.

First, the old VPRM Version used a 3 x 3 spatial smoothing of the MODIS data before the fit, while *pyVPRM* does not. The difference becomes particularly visible for heterogeneous land cover types – in Europe especially for grassland and cropland.

https://doi.org/10.5194/egusphere-2024-3692
Preprint. Discussion started: 21 January 2025
© Author(s) 2025. CC BY 4.0 License.

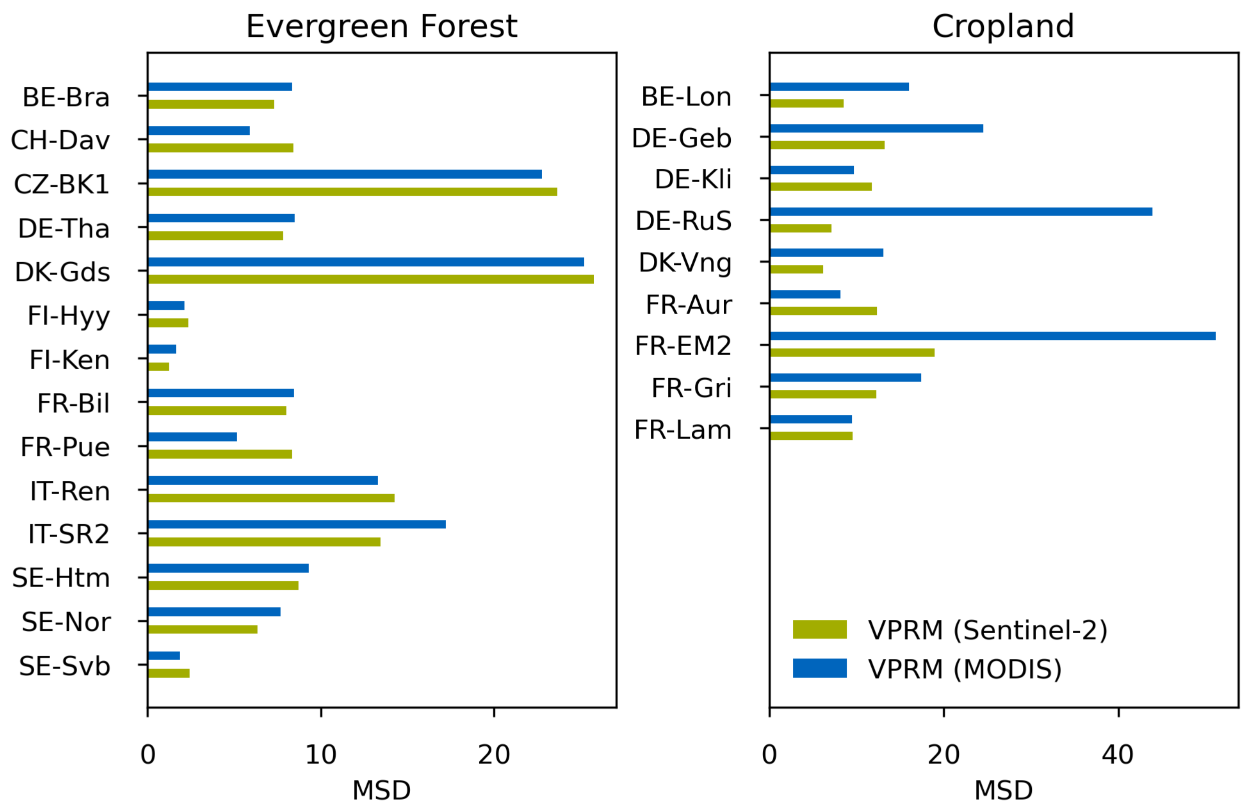

Figure 8. Mean squared deviation (MSD) between the VPRM prediction and the eddy flux tower observation for evergreen forest (left) and cropland sites (right). Different colors show the VPRM predictions using Sentinel-2 and MODIS, respectively.

Figure 9 shows an example of this for the Gebesee (DE-Geb; 51.0997°N, 10.9146°E) cropland site. A single MODIS pixel on top of the flux tower already covers more than one field. Consequently, doing a 3 x 3 pixel smoothing includes many fields, diluting the seasonal cycle of the EVI (see also Fig. 2). As a result, the new GPP model, that does not use spatial smoothing, better matches the observations (Fig. 9).

The second key difference between the versions is that the *pyVPRM* fit follows a two-step procedure: at the beginning the respiration parameters are fitted against nighttime (respiration) measurements and then the GPP parameters are fitted using (daytime) NEE data (utilizing the previously fitted respiration parameters). The old parameters, on the other hand, were produced by simultaneously fitting the GPP and respiration parameters at once using daytime and nighttime NEE data. The problem with this strategy is that errors in the GPP are propagated to the respiration, as GPP fluxes are much larger and more variable than those of respiration. In the case of Gebesee (DE-Geb; 51.0997°N, 10.9146°E), the underestimation of the GPP forces the respiration to also be underestimated to better match the NEE.

https://doi.org/10.5194/egusphere-2024-3692
Preprint. Discussion started: 21 January 2025
© Author(s) 2025. CC BY 4.0 License.

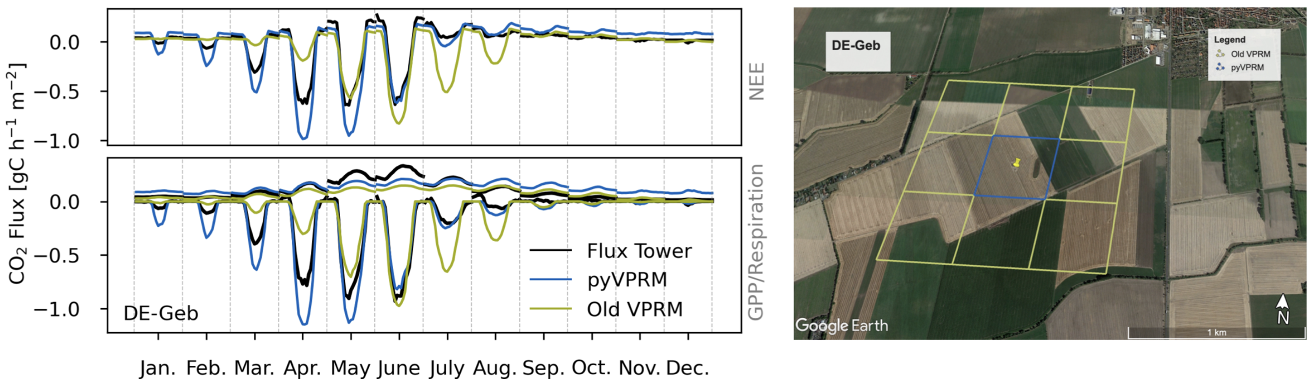

Figure 9. Left panel: The monthly mean diurnal cycles for NEE (top plot), as well as respiration and GPP (bottom plot) for the cropland site Gebesee (DE-Geb; 51.0997°N, 10.9146°E) in 2007. Flux tower data are shown as solid black lines, VPRM estimates from the old and new model are shown as green and blue lines, respectively. The flux partitioning is based on the night-time partitioning method with variable u* threshold. GPP is shown as negative fluxes (carbon uptake) and respiration as positive values (carbon release). Right panel: Image of the site DE-Geb. The white square shows the MODIS pixel on top of the flux tower location (yellow pin). The green pixels show the satellite data used in the previous VPRM version. Map data ©2024 Google.

In summary, this shows that it is important to 1.) match the spatial smoothing of the satellite data to the flux tower footprint and 2.) to fit respiration and GPP separately to avoid systematic biases. As a consequence, the slope of the new respiration function, α in Eq. (9), is three times higher for grasslands and croplands than the previously reported parameters (Gerbig, 2024). Figure 10 shows the respiration function for the grasslands sites for the old and the new version of VPRM (the same plot for the cropland sites is shown in appendix, Fig. E1). The respiration function in the old version underestimates the carbon release to the atmosphere for most of the sites. The deviation becomes especially large for high respiration periods (i.e. high temperature periods). While it is evident that the simple linear respiration function does not capture all effects of the ecosystem respiration the new function is clearly improving over the old version. This has large implications for European flux estimates, as croplands and grassland make up 39% and 15% of the total European land surface area, respectively (Buchhorn et al., 2020).

Overall the annual NEE budget for the European domain in 2023 changes by 75%, from -2.1 PgC yr^{-1} for (ICOS Carbon Portal (Gerbig and Koch, 2024)) to -0.45 PgC yr^{-1} (new *pyVPRM* estimate). The former is likely an overestimation of the carbon sink, caused by the underestimation of respiration. Our new *pyVPRM* budget, on the contrary, is more consistent with previous works estimating the European carbon sink (Monteil et al., 2020; Munassar et al., 2022; Crowell et al., 2019; Scholze et al., 2019). Monteil et al. (2020) provides a comprehensive intercomparison study of different inversion systems with varying transport models, inversion approaches, and priors for the European domain. For most prior biogenic flux models the estimate carbon sink is between -0.5 and 0 PgC yr^{-1}. A much larger sink is only estimated when using the old VPRM fluxes as prior, which is likely related to the respiration issue discussed above. By assimilating three datasets (in situ atmospheric CO_2,

https://doi.org/10.5194/egusphere-2024-3692
Preprint. Discussion started: 21 January 2025
© Author(s) 2025. CC BY 4.0 License.

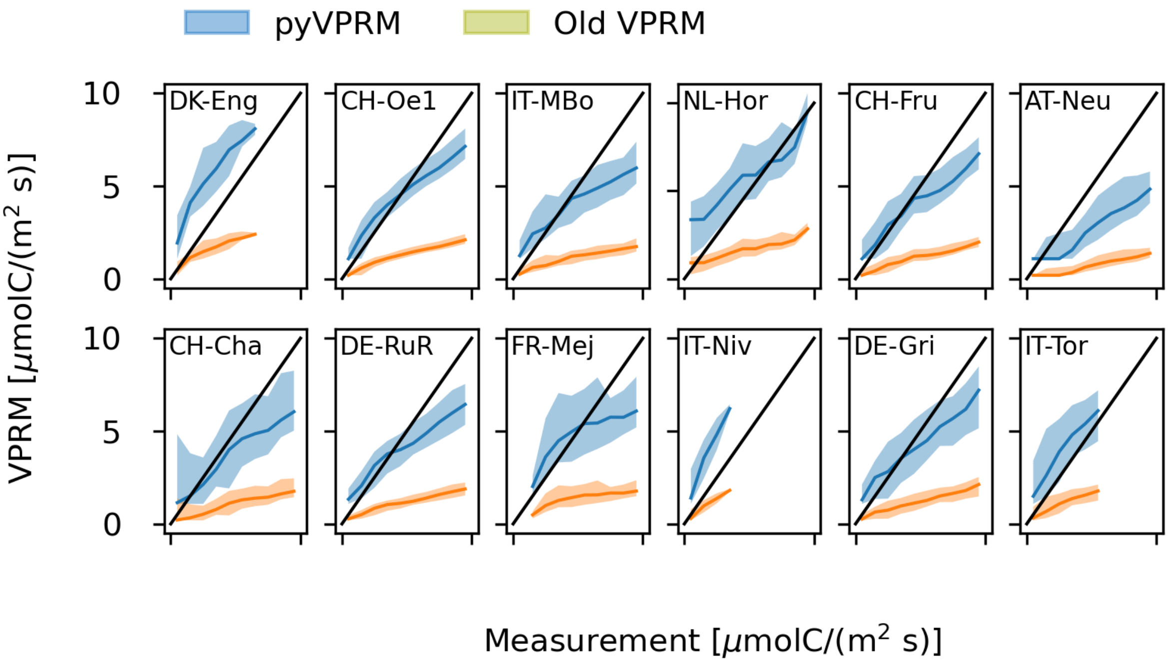

Figure 10. Comparison of VPRM respiration models and eddy-covariance measurements for old VPRM model and the new *pyVPRM* model at the grassland sites. For the measurements data the partitioned variable *'RECO_NT_VUT_REF'* has been used. The bands show the 10% and 90% quantiles of the model. The black solid line is the expectation for a perfect model.

remotely sensed soil moisture and vegetation optical depth) Scholze et al. (2019) estimate a carbon sink of -0.3 ± 0.08 PgC yr^{-1}. Crowell et al. (2019) use OCO-2 XCO2 data in an inversion system an estimate the sink as -0.25 ± 0.46 PgC yr^{-1}.

As expected, the changes from the old to the new VPRM estimate are mainly driven by changes in the budget of grassland and cropland. In both cases the carbon sink decreases by around 0.7 PgC yr^{-1}. Cropland is estimated to be a sink with -0.16 PgC yr^{-1}. Grassland, on the contrary, turns into a source of around 0.4 PgC yr^{-1}. This is clearly visible in Scandinavia, around the Mediterranean and Northern Africa. Assuming a closed carbon cycle this is an indication that some model issues also remain in the new VPRM version. As a second order effect the sink of evergreen forests is reduced by around 0.4 PgC yr^{-1}.

There are different limitations in the current VPRM model that could explain inaccuracies: 1.) the sparse coverage of eddy-covariance towers, especially in Scandinavia, Spain, and the Balkans, does not provide strong constraints on the VPRM parameters in these regions; 2.) the linear respiration function is likely unrealistic for high temperatures and low soil moisture levels. Recent studies suggest that unimodal respiration functions might provide a better description under these conditions (Niu et al., 2024); 3.) the respiration function currently does not take into account the total amount of plants and biomass available. This problem can be tackled by including EVI in the respiration as shown in (Gourdji et al., 2022). An implementation of this mod-

https://doi.org/10.5194/egusphere-2024-3692
Preprint. Discussion started: 21 January 2025
© Author(s) 2025. CC BY 4.0 License.

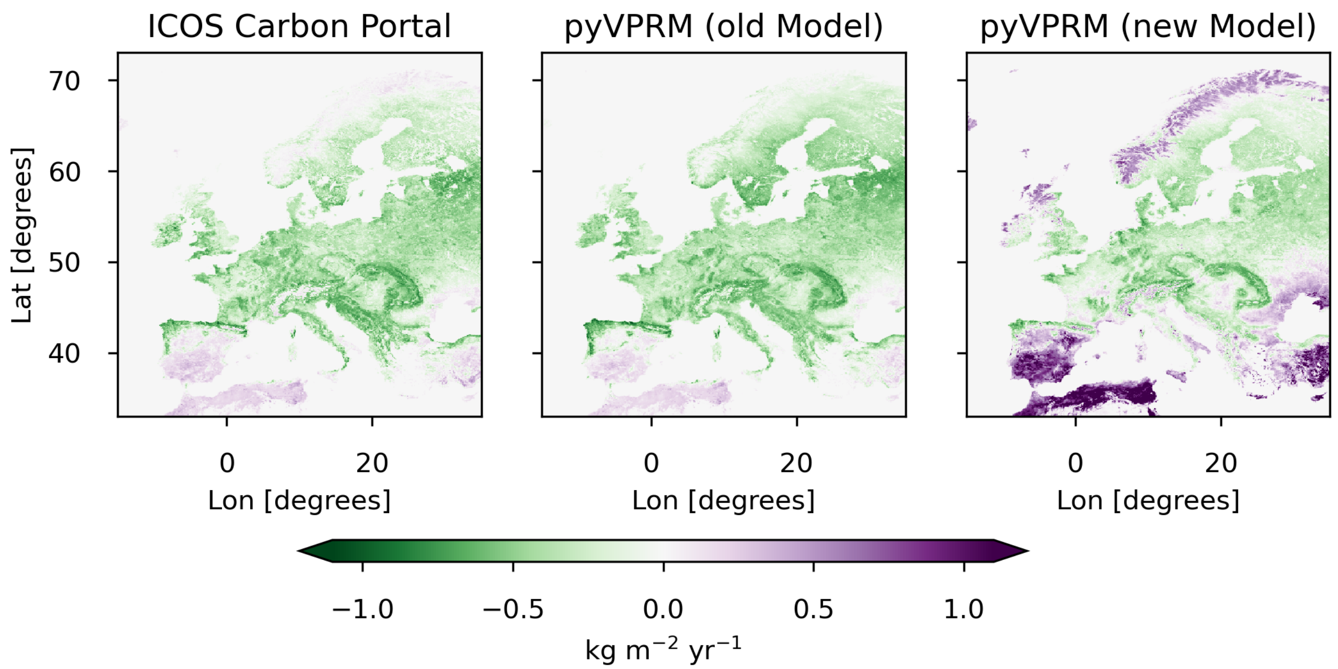

Figure 11. Annual NEE for Europe in 2023 at a 0.25° x 0.25° resolution. Negative flux values (green) show a net carbon uptake, positive values (purple) a net carbon release. Left: Fluxes taken from the ICOS Carbon Portal (Gerbig and Koch, 2024). Middle: Fluxes generated with *pyVPRM* but using the same VPRM parameters and land cover map (SYNMAP) as for the fluxes on the ICOS Carbon Portal. Right: Fluxes calculated using the new *pyVPRM* implementation with the new land cover map and MODIS VPRM parameters as given in Table 3.

ified VPRM is available in the *pyVPRM* Github repository[4] but not discussed in this paper. Improvements for the respiration function will be investigated and implemented in future versions of *pyVPRM*.

	ICOS Carbon Portal	*pyVPRM* (old model)	*pyVPRM* (new model)
Satellite Product	MODIS MOD09A1 version 6.1	MODIS MOD09GA version 6.1	MODIS MOD09GA version 6.1
Land Cover Map	SYNMAP	SYNMAP	Copernicus Dynamic Land Cover Collection 3
Meteorology	ECMWF IFS (three hourly)	ECMWF ERA5-Land (hourly)	ECMWF ERA5-Land (hourly)
VPRM Parameters	VPRM optimization code version Rev.7 (using 3 x 3 pixel smoothing)	VPRM optimization code version Rev.7 (using 3 x 3 pixel smoothing)	*pyVPRM* v3.0 (no spatial smoothing)

Table 4. A comparison of the VPRM settings used to estimate the European carbon fluxes in Fig. 11.

[4]https://github.com/tglauch/pyVPRM/tree/main

https://doi.org/10.5194/egusphere-2024-3692
Preprint. Discussion started: 21 January 2025
© Author(s) 2025. CC BY 4.0 License.

A central improvement of *pyVPRM* is the ability to use different satellite and land cover data products depending on the application. While MODIS and VIIRS provide long term observations at 500-m resolution, Sentinel-2 is especially applicable for high-resolution applications like modeling of urban fluxes. Especially for heterogeneous land cover types like cropland and grassland we significantly improve the estimation of the VPRM parameters and the match with station data. In the future, the parameter estimation can be further improved by taking into account the (time-dependent) footprint of the eddy-covariance towers.

7 Conclusions

pyVPRM provides a next-generation framework for the application of the Vegetation Photosynthesis and Vegetation Model (VPRM) from city to continental-scale. The model is driven by remote sensing indices and meteorological variables to estimate the ecosystem's light-use efficiency for the uptake of carbon through photosynthesis and the (temperature-dependent) ecosystem respiration. Typical applications are the estimation of ecosystem carbon budgets from city to global scale and as biospheric prior for the estimation of both biogenic and anthropogenic CO_2 emissions using atmospheric inversion with transport models like WRF-GHG (Beck et al., 2012) or ICON-ART (Schröter et al., 2018).

pyVPRM extends previous VPRM versions (Mahadevan et al., 2008) by including the latest remote sensing products from Sentinel-2 and VIIRS, as well as updated and dynamic land cover products like the global Copernicus Dynamic Land Cover Collection 3 and the global ESA World Cover. Using Sentinel-2 data enables us, for the first time, to resolve very heterogeneous landscapes like croplands, agricultural grasslands or urban areas. Using VIIRS as a replacement for MODIS guarantees consistent long-term datasets after the planned discontinuation of MODIS. Furthermore, *pyVPRM* brings improvements in the model parameterization of grass- and shrublands compared to current implementation in the ICOS Carbon Portal (Gerbig, 2024).

Free model parameters for eight ecosystem types are fitted using data from up to 97 eddy-covariance towers across Europe. Comparing to flux tower data we observe significant improvements with the Sentinel-2 model, due to a better representation of the flux tower footprint. This is most important for cropland and grassland sites which are heterogeneous vegetation classes that are very abundant in Europe.

In contrast to previous MODIS-based flux estimates for the European domain (Gerbig and Koch, 2021), *pyVPRM* has a more realistic overall budget when compared to independent top-down estimates (Monteil et al., 2020) and improves the seasonal and diunal cycle for grassland and cropland. This is mostly related to the improved fitting procedure in which the estimation of the respiration function is not influenced by mismatches between the measured GPP and the EVI estimation. Smaller improvements come from the usage of a higher resolution land-cover map and the replacement of the 3-hourly ECMWF IFS model (Roberts et al., 2018) with the hourly and higher resolution ERA5-Land re-analysis (Muñoz Sabater et al., 2021).

Due to its modular structure, *pyVPRM* can be easily extended to incorporate other satellite missions, meteorologies models and land cover classifications. Likewise, different versions of the VPRM model can be implemented, examples include the modified VPRM that includes non-linear respiration terms (Gourdji et al., 2022) or the urban VPRM, which has been optimized

https://doi.org/10.5194/egusphere-2024-3692
Preprint. Discussion started: 21 January 2025
© Author(s) 2025. CC BY 4.0 License.

for applications inside of urban areas. (Hardiman et al., 2017). Likewise, we can use the *pyVPRM* framework to run machine-learning-based models.

Code and data availability. The main software framework, *pyVPRM*, can be accessed through Github: https://github.com/tglauch/pyVPRM/tree/main. For the work carried out in this paper the*pyVPRM*release version 3.0 (v3.0) was used. MODIS and VIIRS data are available through https://e4ftl01.cr.usgs.gov/ (visited 2024-09-11). The Copernicus Dynamic Land Cover Service Collection 3 can be accessed through https://lcviewer.vito.be/download (visited 2024-09-11). ESA World Cover data are available under https://esa-worldcover.org/en (visited 2024-09-11). Fluxnet data can be downloaded from https://fluxnet.org/data/fluxnet2015-dataset/ (visited 2024-09-11) and ICOS tower data from https://www.icos-cp.eu/data-products/ecosystem-release (visited 2024-09-11).

Appendix A: Code Structure

For examples on how *pyVPRM* can be used, hands-on example scripts are available on Github[5]. Here, we provide a brief overview of the classes and scripts provided within *pyVPRM*. Two main libraries provide the interface for accessing and pre-processing the required meteorological and satellite data, pyVPRM/meteorologies and pyVPRM/sat_managers, respectively. The main pre-processing of the satellite data and land cover maps is done in the VPRM class, defined in VPRM.py. This is necessary for any kind of VPRM usage. The modules of different VPRM flux models and parameter-fitting functions are defined in the scripts in pyVPRM/vprm_models/, such as pyVPRM/vprm_models/vprm_base.py for the 'base' version of the model. The interface to work with flux tower data used for parameter fitting is given in pyVPRM/lib/flux_tower_class.py, and some useful functions are provided in pyVPRM/lib/functions.py. More details about the scripts/libraries the functions therein are provided below.

pyVPRM/meteorologies

The met_data_handler classes in this folder provide an interface for the input meteorological data, which need to be customized if using a different model or data source. All meteorology classes are derived from the base class in met_base_class.py. An example to implement a new meteorology class can be found in era5_class_draft.py. met_local_measurement.py is used to extract and use site-level meteorological data.

pyVPRM/sat_managers

The satellite_data_manager class in this library is the basic data structure for all satellite image and land cover maps used in *pyVPRM*. It provides functions to reproject, transform, merge and crop satellite images. All other classes for specific satellite images or land cover maps, with their respective loading routines, are derived from this base class and implemented in the respective class files in the folder.

[5]https://github.com/tglauch/pyVPRM_examples/tree/main

The other scripts in this library define classes for specific satellite reflectance products (modis.py, proba_v.py, sentinel2.py, viirs.py, viirs09ga.py) or land cover maps (city.py, copernicus.py, esa_world_cover.py, mapbiomas.py, synmap.py), along with product-specific functions for data screening (e.g. for clouds, snow, bad pixels). Configuration (yaml) files describing different the categories for different land cover maps are found in pyVPRM/vprm_configs and are required to map the land cover categories to VPRM classes.

VPRM.py

The VPRM class defined in VPRM.py is the implementation of the VPRM preprocessor. This is the central code to calculate the satellite indices, run the time smoothing, transform satellite data and land cover map to the same grid and prepare all the variables for the VPRM models. It can also be used to generate input files to run VPRM online in atmospheric models. In order to run the preprocessor, a configuration file with a mapping from land cover classes to VPRM classes is required.

pyVPRM/vprm_models/vprm_base.py

In this folder, different implementations of the VPRM model are included. Every implementation requires at least a function to fit the VPRM parameters and make VPRM predictions given an instance of the VPRM preprocessor and the meteorology. The version described throughout this paper is in vprm_base.py.

pyVPRM/lib/flux_tower_class.py

Flux tower data are not completely harmonized in terms of format, and as such, custom classes will likely need to be added to accommodate new data sources, and vegetation classes/land cover types may need to be harmonized by hand. Custom classes are included in this script already for FLUXNET, ICOS, AmeriFlux, and the LBA-ECO CD-32 Flux Tower Network Data Compilation. This can also be used as a template for adding new flux tower sites.

pyVPRM/lib/functions.py

Additional functions that are used in *pyVPRM* are stored in functions.py.

https://doi.org/10.5194/egusphere-2024-3692
Preprint. Discussion started: 21 January 2025
© Author(s) 2025. CC BY 4.0 License.

Appendix B: Data quality masking

	MODIS
Band quality masking	Highest quality surface Reflectance Band Quality Description (0000) for band 1, band 2, band 3, band 6
Clouds Masking	State QA flag 0-1 (cloud state) == 00 (clear) and State QA flag 8-9 (cirrus detected) == 00 (none)
Cloud Shadow Masking	State QA flag 2 (cloud shadow) == 0 (no)
Snow Masking	State QA flag 12 (MOD35 snow/ice flag) == 0 (no)

Table B1. Flags used for data masking in MODIS. Scenes where any of the band quality, clouds masking or cloud shadow masking criteria are not fulfilled are masked out. Scenes with active snow flag have a special treatment, see Sect. 3.1.3

	VIIRS
Band quality masking	Highest quality surface Reflectance Band Quality Description (0000) for band 1, band 2, band 3
Clouds Masking	State QA flag 0-1 (cloud state) == 00 (clear) and State QA flag 8-9 (cirrus detected) == 00 (none)
Cloud Shadow Masking	State QA flag 2 (cloud shadow) == 0 (no)
Snow Masking	State QA flag 12 (MOD35 snow/ice flag) == 0 (no)

Table B2. Flags used for data masking in VIIRS. Scenes where any of the band quality, clouds masking or cloud shadow masking criteria are not fulfilled are masked out. Scenes with active snow flag have a special treatment, see Sect. 3.1.3.

	Sentinel-2
Band quality masking	SCL Flag not 0,1,2
Clouds Masking	SCL Flag not 8,9, 10
Cloud Shadow Masking	SCL Flag not 3
Snow Masking	SCL Flag not 11

Table B3. Flags used for data masking in Sentinel-2. Scenes where any of the band quality, clouds masking or cloud shadow masking criteria are not fulfilled are masked out. Scenes with active snow flag have a special treatment, see Sect. 3.1.3

https://doi.org/10.5194/egusphere-2024-3692
Preprint. Discussion started: 21 January 2025
© Author(s) 2025. CC BY 4.0 License.

Appendix C: Flux Tower Data

Site Name	Veg. Type	Longitude [°E]	Latitude [°N]	Data Year
AT-Neu	GRA	11.32	47.12	2010
BE-Bra	EF	4.52	51.31	2022
BE-Lcr	DF	3.85	51.11	2020
BE-Lon	CRO	4.75	50.55	2020
BE-Maa	SH	5.63	50.98	2022
BE-Vie	MF	6.00	50.30	2022
CH-Cha	GRA	8.41	47.21	2013
CH-Dav	EF	9.86	46.82	2022
CH-Fru	GRA	8.54	47.12	2008
CH-Lae	MF	8.36	47.48	2014
CH-Oe1	GRA	7.73	47.29	2007
CH-Oe2	CRO	7.73	47.29	2009
CZ-BK1	EF	18.54	49.50	2022
CZ-BK2	GRA	18.54	49.49	2004
CZ-Lnz	DF	16.95	48.68	2022
CZ-wet	WET	14.77	49.02	2020
DE-Akm	WET	13.68	53.87	2010
DE-Geb	CRO	10.91	51.10	2007
DE-Geb	CRO	10.91	51.10	2021
DE-Gri	GRA	13.51	50.95	2021
DE-Hai	DF	10.45	51.08	2020
DE-Har	MF	7.60	47.93	2021
DE-HoH	DF	11.22	52.09	2022
DE-Kli	CRO	13.52	50.89	2020
DE-Lkb	EF	13.30	49.10	2011
DE-Lnf	DF	10.37	51.33	2008
DE-Msr	EF	11.46	47.81	2021
DE-Obe	EF	13.72	50.79	2012
DE-RuR	GRA	6.30	50.62	2015
DE-RuS	CRO	6.45	50.87	2022
DE-RuW	EF	6.33	50.50	2012
DE-Seh	CRO	6.45	50.87	2009

Table C1. Flux tower sites used for estimating the MODIS VPRM parameters. Table 1/3.

https://doi.org/10.5194/egusphere-2024-3692
Preprint. Discussion started: 21 January 2025
© Author(s) 2025. CC BY 4.0 License.

Site Name	Veg. Type	Latitude [°N]	Longitude [°E]	Data Year
DE-SfN	WET	11.33	47.81	2014
DE-Spw	WET	14.03	51.89	2012
DE-Tha	EF	13.57	50.96	2022
DE-Zrk	WET	12.89	53.88	2014
DK-Eng	GRA	12.19	55.69	2006
DK-Fou	CRO	9.59	56.48	2005
DK-Gds	EF	9.33	56.07	2021
DK-Skj	WET	8.40	55.91	2022
DK-Sor	DF	11.64	55.49	2022
DK-Vng	CRO	9.16	56.04	2022
ES-Amo	SH	-2.25	36.83	2009
ES-LJu	SH	-2.75	36.93	2009
ES-LgS	SH	-2.97	37.10	2008
ES-Ln2	SH	-3.48	36.97	2009
FI-Hyy	EF	24.29	61.85	2019
FI-Jok	CRO	23.51	60.90	2001
FI-Ken	EF	24.24	67.99	2020
FI-Let	EF	23.96	60.64	2017
FI-Lom	WET	24.21	68.00	2008
FI-Sii	WET	24.19	61.83	2019
FI-Sod	EF	26.64	67.36	2011
FI-Var	EF	29.61	67.75	2018
FR-Aur	CRO	1.11	43.55	2021
FR-Bil	EF	-0.96	44.49	2022
FR-EM2	CRO	3.02	49.87	2020
FR-Fon	DF	2.78	48.48	2020
FR-Gri	CRO	1.95	48.84	2022
FR-Hes	DF	7.06	48.67	2022
FR-LBr	EF	-0.77	44.72	2002
FR-LGt	WET	2.28	47.32	2020
FR-Lam	CRO	1.24	43.50	2022
FR-Mej	GRA	-1.80	48.12	2020
FR-Pue	EF	3.60	43.74	2022
FR-Tou	GRA	1.37	43.57	2020
IT-BCi	CRO	14.96	40.52	2007

Table C2. Flux tower sites used for estimating the MODIS VPRM parameters. Table 2/3.

https://doi.org/10.5194/egusphere-2024-3692
Preprint. Discussion started: 21 January 2025
© Author(s) 2025. CC BY 4.0 License.

Site Name	Veg. Type	Latitude [°N]	Longitude [°E]	Data Year
IT-BFt	DF	10.74	45.20	2021
IT-CA1	DF	12.03	42.38	2012
IT-CA2	CRO	12.03	42.38	2012
IT-CA3	DF	12.02	42.38	2013
IT-Col	DF	13.59	41.85	2014
IT-Cp2	MF	12.36	41.70	2022
IT-Cpz	EF	12.38	41.71	2000
IT-Isp	DF	8.63	45.81	2014
IT-La2	EF	11.29	45.95	2001
IT-Lav	EF	11.28	45.96	2013
IT-Lsn	SH	12.75	45.74	2018
IT-MBo	GRA	11.05	46.01	2007
IT-Niv	GRA	7.14	45.49	2020
IT-Noe	SH	8.15	40.61	2010
IT-PT1	DF	9.06	45.20	2003
IT-Ren	EF	11.43	46.59	2022
IT-Ro1	DF	11.93	42.41	2006
IT-Ro2	DF	11.92	42.39	2009
IT-SR2	EF	10.29	43.73	2021
IT-SRo	EF	10.28	43.73	2004
IT-Tor	GRA	7.58	45.84	2022
NL-Hor	GRA	5.07	52.24	2007
NL-Loo	EF	5.74	52.17	2006
SE-Deg	WET	19.56	64.18	2020
SE-Htm	EF	13.42	56.10	2022
SE-Nor	EF	17.48	60.09	2020
SE-St1	WET	19.05	68.35	2013
SE-Sto	WET	19.05	68.36	2022
SE-Svb	EF	19.77	64.26	2020
SJ-Adv	WET	15.92	78.19	2011
UK-AMo	WET	-3.24	55.79	2022

Table C3. Flux tower sites used for estimating the MODIS VPRM parameters. Table 3/3.

https://doi.org/10.5194/egusphere-2024-3692
Preprint. Discussion started: 21 January 2025
© Author(s) 2025. CC BY 4.0 License.

Site Name	Veg. Type	Latitude [°N]	Longitude [°E]	Data Year
BE-Bra	EF	4.52	51.31	2022
BE-Lcr	DF	3.85	51.11	2020
BE-Lon	CRO	4.75	50.55	2020
BE-Maa	SH	5.63	50.98	2022
BE-Vie	MF	6.00	50.30	2022
CH-Dav	EF	9.86	46.82	2022
CZ-BK1	EF	18.54	49.50	2022
CZ-Lnz	DF	16.95	48.68	2022
CZ-wet	WET	14.77	49.02	2020
DE-Geb	CRO	10.91	51.10	2021
DE-Gri	GRA	13.51	50.95	2021
DE-Hai	DF	10.45	51.08	2020
DE-Har	MF	7.60	47.93	2021
DE-HoH	DF	11.22	52.09	2022
DE-Kli	CRO	13.52	50.89	2020
DE-Msr	EF	11.46	47.81	2021
DE-RuR	GRA	6.30	50.62	2020
DE-RuS	CRO	6.45	50.87	2022
DE-RuW	EF	6.33	50.50	2020
DE-Tha	EF	13.57	50.96	2022
DK-Gds	EF	9.33	56.07	2021
DK-Skj	WET	8.40	55.91	2022
DK-Sor	DF	11.64	55.49	2022
DK-Vng	CRO	9.16	56.04	2022
FI-Hyy	EF	24.29	61.85	2019
FI-Ken	EF	24.24	67.99	2020
FI-Let	EF	23.96	60.64	2018
FI-Sii	WET	24.19	61.83	2019
FR-Aur	CRO	1.11	43.55	2021
FR-Bil	EF	-0.96	44.49	2022
FR-EM2	CRO	3.02	49.87	2020
FR-Fon	DF	2.78	48.48	2020
FR-Gri	CRO	1.95	48.84	2022
FR-Hes	DF	7.06	48.67	2022
FR-LGt	WET	2.28	47.32	2020

Table C4. Flux tower sites used for estimating the Sentinel-2 VPRM parameters. Table 1/2.

https://doi.org/10.5194/egusphere-2024-3692
Preprint. Discussion started: 21 January 2025
© Author(s) 2025. CC BY 4.0 License.

Site Name	Veg. Type	Latitude [°N]	Longitude [°E]	Data Year
FR-LGt	WET	2.28	47.32	2020
FR-Lam	CRO	1.24	43.50	2022
FR-Mej	GRA	-1.80	48.12	2020
FR-Pue	EF	3.60	43.74	2022
FR-Tou	GRA	1.37	43.57	2020
IT-BFt	DF	10.74	45.20	2021
IT-Cp2	MF	12.36	41.70	2022
IT-Lsn	SH	12.75	45.74	2018
IT-Niv	GRA	7.14	45.49	2020
IT-Ren	EF	11.43	46.59	2022
IT-SR2	EF	10.29	43.73	2021
IT-Tor	GRA	7.58	45.84	2022
SE-Deg	WET	19.56	64.18	2020
SE-Htm	EF	13.42	56.10	2022
SE-Nor	EF	17.48	60.09	2020
SE-Sto	WET	19.05	68.36	2022
SE-Svb	EF	19.77	64.26	2020
UK-AMo	WET	-3.24	55.79	2022

Table C5. Flux tower sites used for estimating the Sentinel-2 VPRM parameters. Table 2/2.

https://doi.org/10.5194/egusphere-2024-3692
Preprint. Discussion started: 21 January 2025
© Author(s) 2025. CC BY 4.0 License.

Site Name	Veg. Type	Latitude [°N]	Longitude [°E]	Data Year
BE-Bra	EF	4.52	51.31	2022
BE-Lcr	DF	3.85	51.11	2020
BE-Lon	CRO	4.75	50.55	2020
BE-Maa	SH	5.63	50.98	2022
BE-Vie	MF	6.00	50.30	2022
CH-Cha	GRA	8.41	47.21	2013
CH-Dav	EF	9.86	46.82	2022
CH-Fru	GRA	8.54	47.12	2013
CH-Lae	MF	8.36	47.48	2014
CH-Oe2	CRO	7.73	47.29	2013
CZ-BK1	EF	18.54	49.50	2022
CZ-Lnz	DF	16.95	48.68	2022
CZ-wet	WET	14.77	49.02	2020
DE-Akm	WET	13.68	53.87	2013
DE-Geb	CRO	10.91	51.10	2021
DE-Gri	GRA	13.51	50.95	2021
DE-Hai	DF	10.45	51.08	2020
DE-Har	MF	7.60	47.93	2021
DE-HoH	DF	11.22	52.09	2022
DE-Kli	CRO	13.52	50.89	2020
DE-Msr	EF	11.46	47.81	2021
DE-RuR	GRA	6.30	50.62	2015
DE-RuS	CRO	6.45	50.87	2022
DE-SfN	WET	11.33	47.81	2014
DE-Tha	EF	13.57	50.96	2022
DE-Zrk	WET	12.89	53.88	2014
DK-Gds	EF	9.33	56.07	2021
DK-Skj	WET	8.40	55.91	2022
DK-Sor	DF	11.64	55.49	2022
DK-Vng	CRO	9.16	56.04	2022
ES-LJu	SH	-2.75	36.93	2013
FI-Hyy	EF	24.29	61.85	2019
FI-Ken	EF	24.24	67.99	2020
FI-Let	EF	23.96	60.64	2017

Table C6. Flux tower sites used for estimating the VIIRS VPRM parameters. Table 1/2.

https://doi.org/10.5194/egusphere-2024-3692
Preprint. Discussion started: 21 January 2025
© Author(s) 2025. CC BY 4.0 License.

Site Name	Veg. Type	Latitude [°N]	Longitude [°E]	Data Year
FI-Sii	WET	24.19	61.83	2019
FI-Sod	EF	26.64	67.36	2013
FI-Var	EF	29.61	67.75	2018
FR-Aur	CRO	1.11	43.55	2021
FR-Bil	EF	-0.96	44.49	2022
FR-EM2	CRO	3.02	49.87	2020
FR-Fon	DF	2.78	48.48	2020
FR-Gri	CRO	1.95	48.84	2022
FR-Hes	DF	7.06	48.67	2022
FR-LGt	WET	2.28	47.32	2020
FR-Lam	CRO	1.24	43.50	2022
FR-Mej	GRA	-1.80	48.12	2020
FR-Pue	EF	3.60	43.74	2022
FR-Tou	GRA	1.37	43.57	2020
IT-BCi	CRO	14.96	40.52	2013
IT-BFt	DF	10.74	45.20	2021
IT-CA3	DF	12.02	42.38	2013
IT-Col	DF	13.59	41.85	2014
IT-Cp2	MF	12.36	41.70	2022
IT-Isp	DF	8.63	45.81	2014
IT-Lav	EF	11.28	45.96	2013
IT-Lsn	SH	12.75	45.74	2018
IT-Niv	GRA	7.14	45.49	2020
IT-Ren	EF	11.43	46.59	2022
IT-SR2	EF	10.29	43.73	2021
IT-Tor	GRA	7.58	45.84	2022
SE-Deg	WET	19.56	64.18	2020
SE-Htm	EF	13.42	56.10	2022
SE-Nor	EF	17.48	60.09	2020
SE-St1	WET	19.05	68.35	2013
SE-Sto	WET	19.05	68.36	2022
SE-Svb	EF	19.77	64.26	2020
SJ-Adv	WET	15.92	78.19	2013
UK-AMo	WET	-3.24	55.79	2022

Table C7. Flux tower sites used for estimating the VIIRS VPRM parameters. Table 2/2.

https://doi.org/10.5194/egusphere-2024-3692
Preprint. Discussion started: 21 January 2025
© Author(s) 2025. CC BY 4.0 License.

465 **Appendix D: Diurnal Cycles for Cropland Sites**

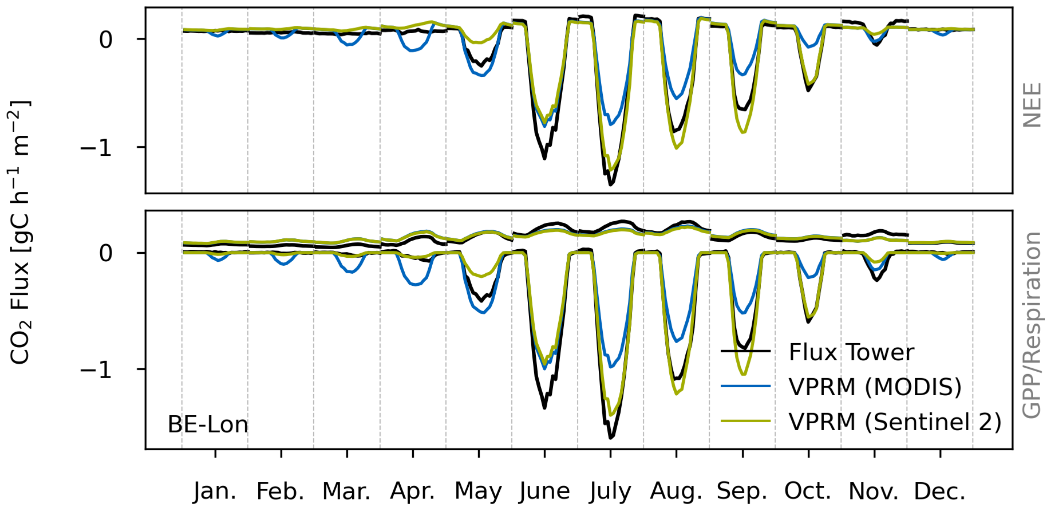

Figure D1. The mean diurnal cycle for each month at the cropland site BE-Lon. The median tower measurements for each hour of the day are shown as black lines. Colored solid lines indicate the results from the VPRM model using indices from Sentinel-2 (green) and MODIS (blue). In the top panel NEE is shown and in the bottom panel GPP (negative values, carbon uptake) and respiration (positive values, carbon release) are shown. The flux partitioning is based on the night-time partitioning method with variable u^* threshold (Reichstein et al., 2005).

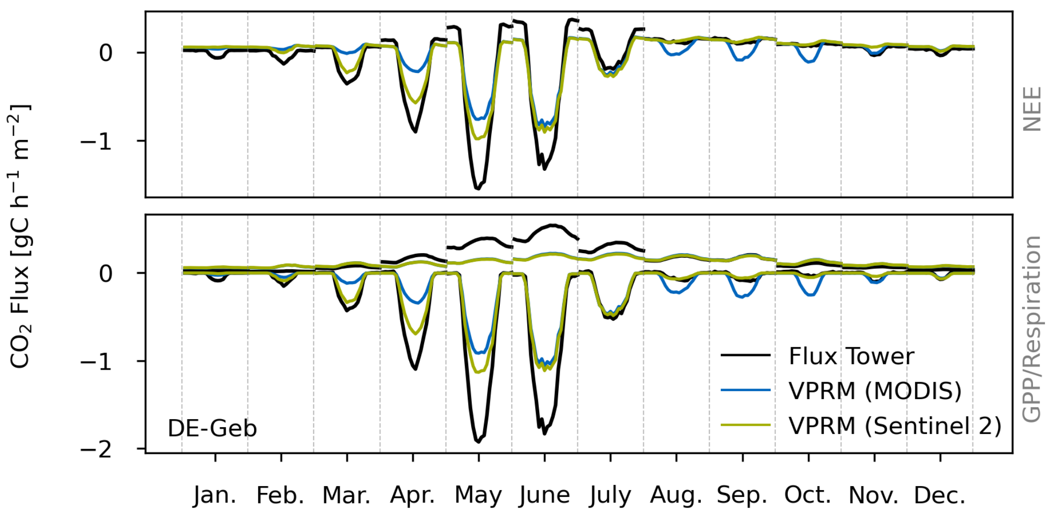

Figure D2. The mean diurnal cycle for each month at the cropland site DE-Geb. For more details see Fig. D1.

https://doi.org/10.5194/egusphere-2024-3692
Preprint. Discussion started: 21 January 2025
© Author(s) 2025. CC BY 4.0 License.

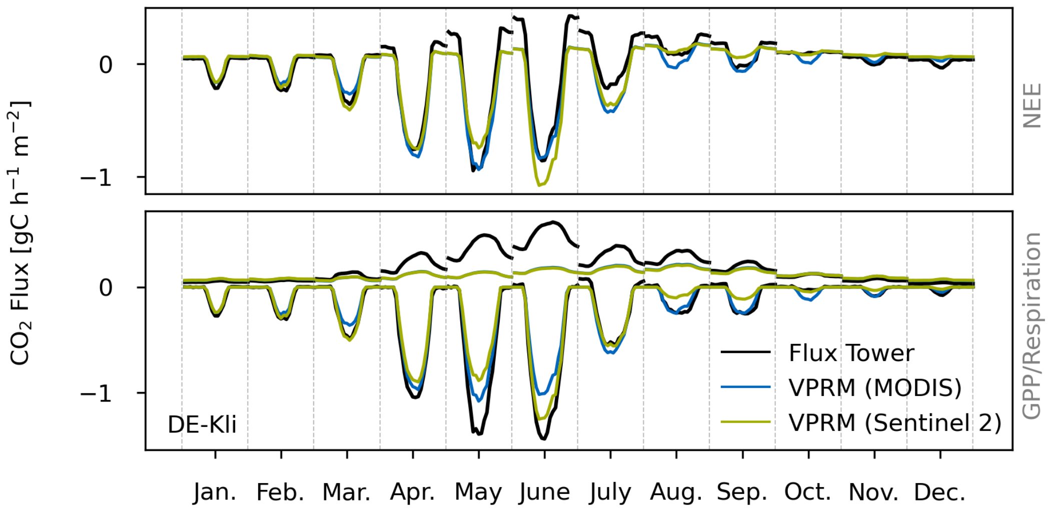

Figure D3. The mean diurnal cycle for each month at the cropland site DE-Kli. For more details see Fig. D1.

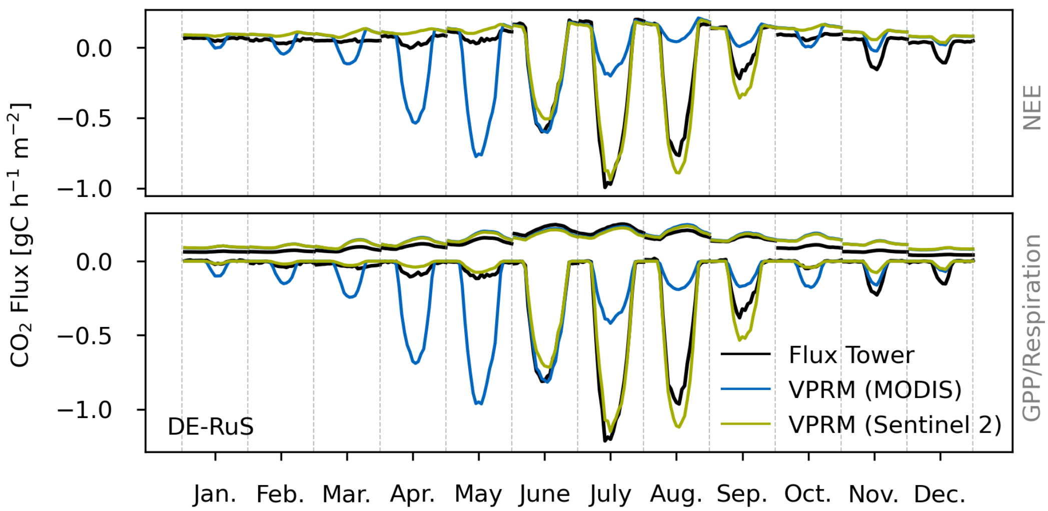

Figure D4. The mean diurnal cycle for each month at the cropland site DE-RuS. For more details see Fig. D1.

https://doi.org/10.5194/egusphere-2024-3692
Preprint. Discussion started: 21 January 2025
© Author(s) 2025. CC BY 4.0 License.

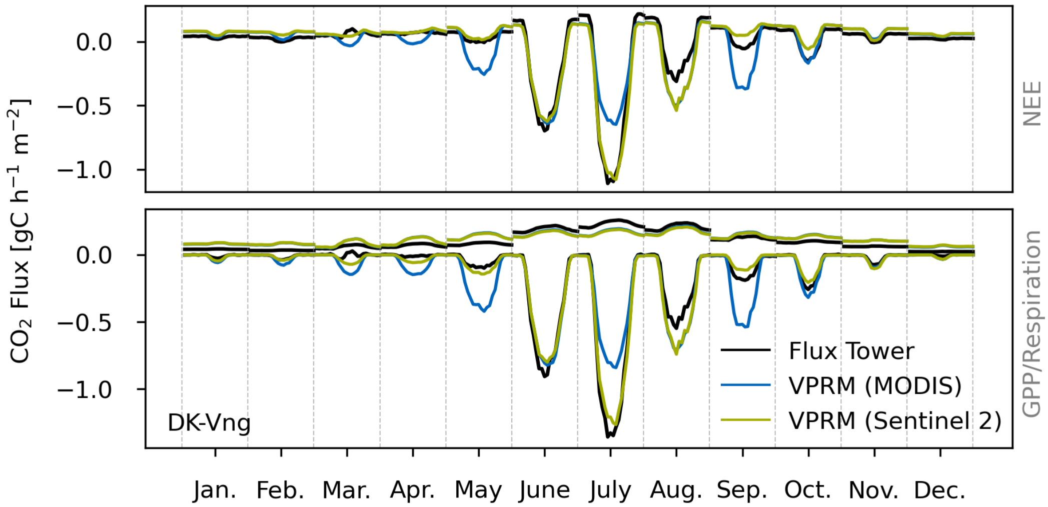

Figure D5. The mean diurnal cycle for each month at the cropland site DK-Vng. For more details see Fig. D1.

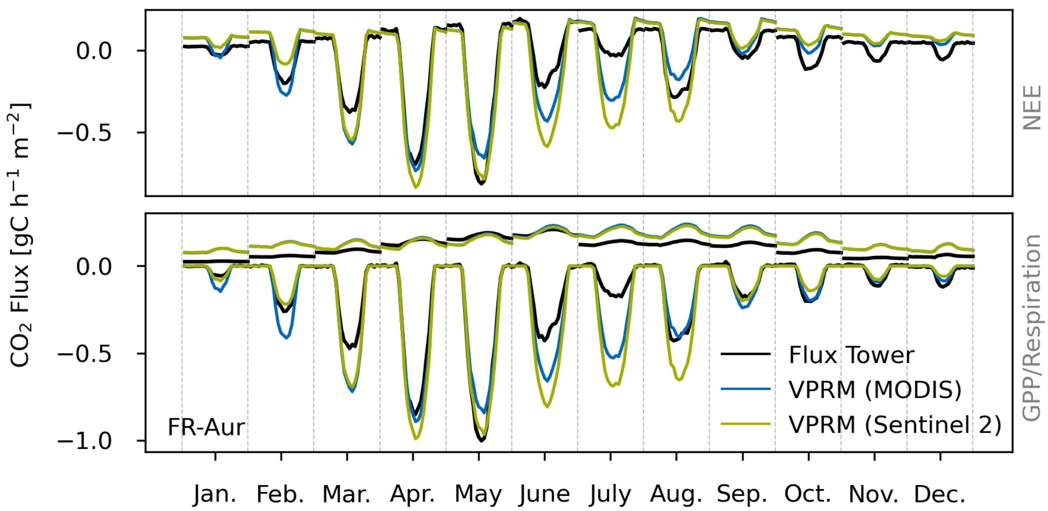

Figure D6. The mean diurnal cycle for each month at the cropland site FR-Aur. For more details see Fig. D1.

https://doi.org/10.5194/egusphere-2024-3692
Preprint. Discussion started: 21 January 2025
© Author(s) 2025. CC BY 4.0 License.

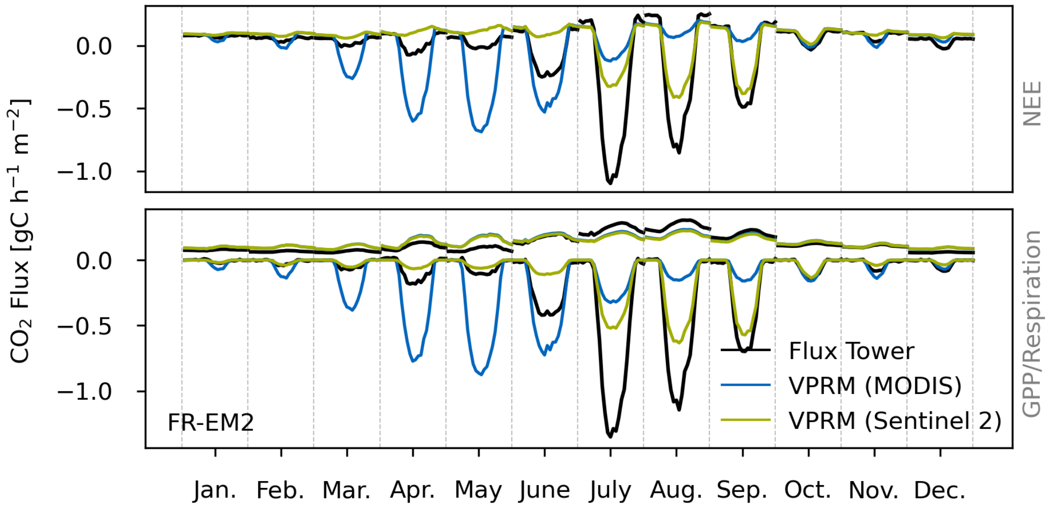

Figure D7. The mean diurnal cycle for each month at the cropland site FR-EM2. For more details see Fig. D1.

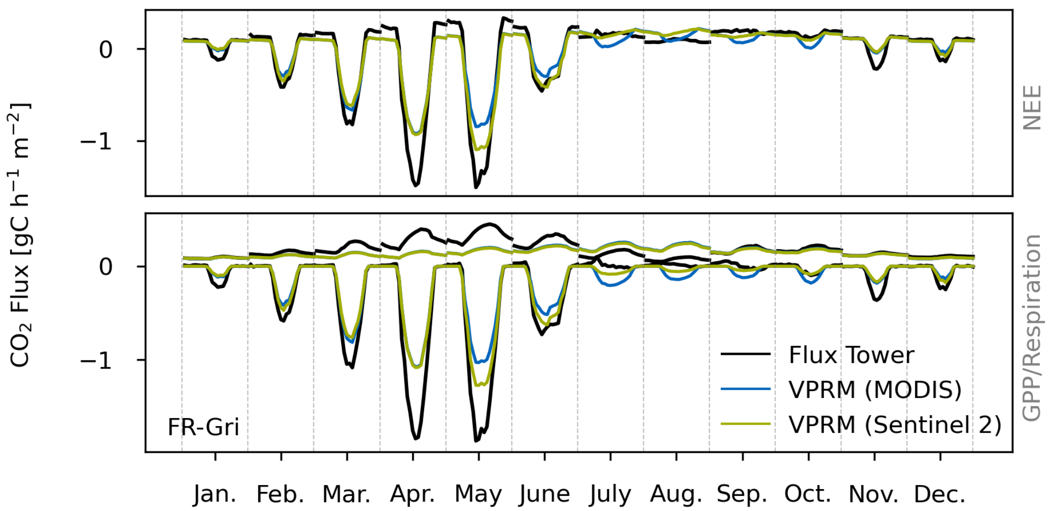

Figure D8. The mean diurnal cycle for each month at the cropland site FR-Gri. For more details see Fig. D1.

https://doi.org/10.5194/egusphere-2024-3692
Preprint. Discussion started: 21 January 2025
© Author(s) 2025. CC BY 4.0 License.

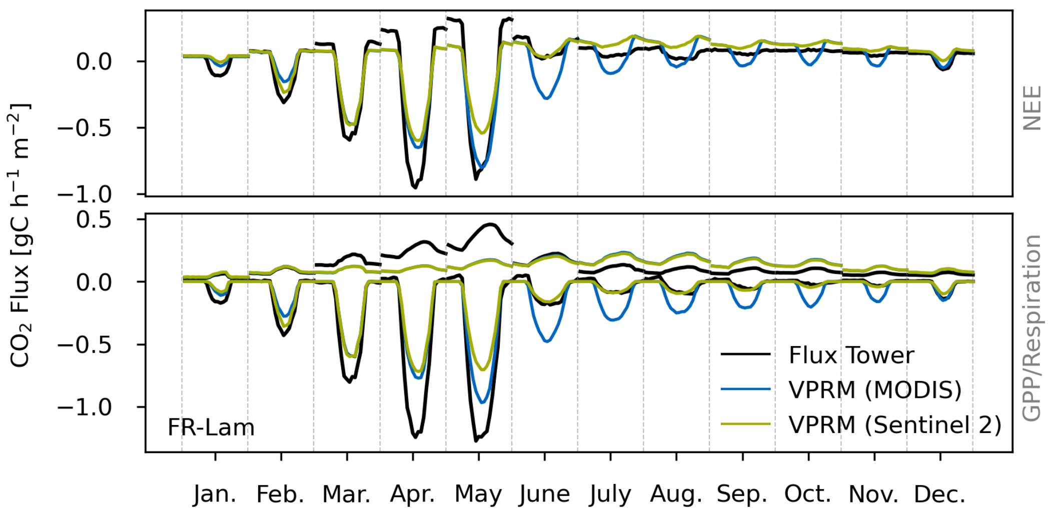

Figure D9. The mean diurnal cycle for each month at the cropland site FR-Lam. For more details see Fig. D1.

https://doi.org/10.5194/egusphere-2024-3692
Preprint. Discussion started: 21 January 2025
© Author(s) 2025. CC BY 4.0 License.

Appendix E: Respiration Functions

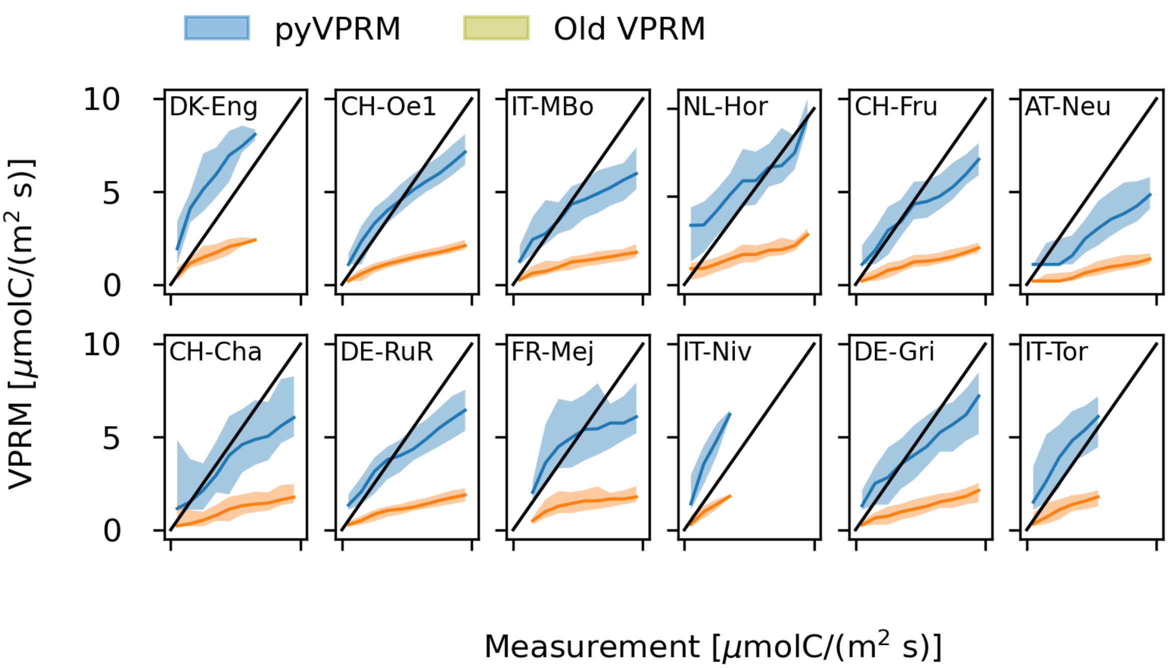

Figure E1. Comparison of VPRM respiration models and eddy-covariance measurements for old VPRM model and the new *pyVPRM* model at the cropland sites. For the measurements data the partitioned variable *'RECO_NT_VUT_REF'* has been used. The bands show the 10% and 90% quantiles of the model. The black solid line is the expectation for a perfect model.

https://doi.org/10.5194/egusphere-2024-3692
Preprint. Discussion started: 21 January 2025
© Author(s) 2025. CC BY 4.0 License.

Appendix F: Old VPRM parameters

	Temperatures				MODIS			
	T_{min}	T_{opt}	T_{max}	T_{low}	λ	par_0	α	β
EF	0	20	40	4	0.20	313.95	0.22	-0.64
DF	0	20	40	0	0.18	313.28	0.13	1.14
MF	0	20	40	2	0.14	514.99	0.17	0.01
SHR	2	20	40	4	0.20	100.98	0.05	-0.17
SAV	2	20	40	0	0.11	682.00	0.005	0
CRO	5	22	40	0	0.08	132.29	0.07	0.58
GRA	2	18	40	0	0.17	579.44	0.09	0.36

Table F1. Overview of the VPRM parameter sets for MODIS used for the fluxes on the ICOS Carbon Portal (Gerbig, 2024) . Abbreviations are as follows: EF - evergreen forest, DF - deciduous forest, MF - mixed forest, SHR - shrubland, SAV - Savanna, CRO - cropland, GRA - grassland

Author contributions. TG developed and implemented the software framework *pyVPRM* and performed the analysis. JM, CG, MG, and AB supervised the work. All authors participated in the interpretation of the results and in the writing and editing of the publication.

Competing interests. The contact author has declared that none of the authors has any competing interests.

Acknowledgements. This work used resources of the Deutsches Klimarechenzentrum (DKRZ) granted by its Scientific Steering Committee (WLA) under project bd1231. The authors also gratefully acknowledge the computational and data resources provided by the Leibniz Supercomputing Centre through the Terrabyte facilities. The work was financed through the CO2KI project of the BMBF (project number FZK50EE2212). This research has been supported by BMBF through the ITMS-M project under contract 01LK2102A. This publication has been prepared using European Union's Copernicus Land Monitoring Service information; 10.5281/zenodo.3939050. We thank Friedemann Reum and Thomas Plewa for useful discussions. We thank the Terrabyte cluster for providing access to Sentinel-2 data.

https://doi.org/10.5194/egusphere-2024-3692
Preprint. Discussion started: 21 January 2025
© Author(s) 2025. CC BY 4.0 License.

References

Ahmadov, R., Gerbig, C., Kretschmer, R., Körner, S., Rödenbeck, C., Bousquet, P., and Ramonet, M.: Comparing high resolution WRF-VPRM simulations and two global CO_2 transport models with coastal tower measurements of CO_2, Biogeosciences, 6, 807–817, https://doi.org/10.5194/bg-6-807-2009, 2009.

Bazzi, H., Ciais, P., Abbessi, E., Makowski, D., Santaren, D., Ceschia, E., Brut, A., Tallec, T., Buchmann, N., Maier, R., Acosta, M., Loubet, B., Buysse, P., Léonard, J., Bornet, F., Fayad, I., Lian, J., Baghdadi, N., Segura Barrero, R., Brümmer, C., Schmidt, M., Heinesch, B., Mauder, M., and Gruenwald, T.: Assimilating Sentinel-2 data in a modified vegetation photosynthesis and respiration model (VPRM) to improve the simulation of croplands CO_2 fluxes in Europe, International Journal of Applied Earth Observation and Geoinformation, 127, 103 666, https://doi.org/10.1016/j.jag.2024.103666, 2024.

Beck, V., Koch, T., Kretschmer, R., Marshall, J., Ahmadov, R., Gerbig, C., Pillai, D., and Heimann, M.: The WRF Greenhouse Gas Model (WRF-GHG). Technical Report No. 25, Tech. rep., Max Planck Institute for Biogeochemistry, Jena, Germany, https://www.bgc-jena.mpg.de/5363366/tech_report25.pdf, 2012.

Bousquet, P., Ciais, P., Peylin, P., Ramonet, M., and Monfray, P.: Inverse modeling of annual atmospheric CO_2 sources and sinks: 1. Method and control inversion, Journal of Geophysical Research: Atmospheres, 104, 26 161–26 178, 1999.

Buchhorn, M., Smets, B., Bertels, L., De Roo, B., Lesiv, M., Tsendbazar, N., Li, L., and Tarko, A.: Copernicus Global Land Service: Land Cover 100m: Version 3 Globe 2015-2019: Product User Manual, Zenodo, https://doi.org/10.5281/zenodo.3938963, 2020.

Chen, B., Black, T. A., Coops, N. C., Hilker, T., Trofymow, J., and Morgenstern, K.: Assessing tower flux footprint climatology and scaling between remotely sensed and eddy covariance measurements, Boundary-layer meteorology, 130, 137–167, 2009.

Cleveland, W. S.: Robust Locally Weighted Regression and Smoothing Scatterplots, Journal of the American Statistical Association, 74, 829–836, https://doi.org/10.1080/01621459.1979.10481038, 1979.

Commane, R., Lindaas, J., Benmergui, J., Luus, K. A., Chang, R. Y.-W., Daube, B. C., Euskirchen, E. S., Henderson, J. M., Karion, A., Miller, J. B., Miller, S. M., Parazoo, N. C., Randerson, J. T., Sweeney, C., Tans, P., Thoning, K., Veraverbeke, S., Miller, C. E., and Wofsy, S. C.: Carbon dioxide sources from Alaska driven by increasing early winter respiration from Arctic tundra, Proceedings of the National Academy of Sciences, 114, 5361–5366, https://doi.org/10.1073/pnas.1618567114, 2017.

Crowell, S., Baker, D., Schuh, A., Basu, S., Jacobson, A. R., Chevallier, F., Liu, J., Deng, F., Feng, L., McKain, K., Chatterjee, A., Miller, J. B., Stephens, B. B., Eldering, A., Crisp, D., Schimel, D., Nassar, R., O'Dell, C. W., Oda, T., Sweeney, C., Palmer, P. I., and Jones, D. B. A.: The 2015–2016 carbon cycle as seen from OCO-2 and the global in situ network, Atmospheric Chemistry and Physics, 19, 9797–9831, https://doi.org/10.5194/acp-19-9797-2019, 2019.

Dayalu, A., Munger, J. W., Wofsy, S. C., Wang, Y., Nehrkorn, T., Zhao, Y., McElroy, M. B., Nielsen, C. P., and Luus, K.: Assessing biotic contributions to CO_2 fluxes in northern China using the Vegetation, Photosynthesis and Respiration Model (VPRM-CHINA) and observations from 2005 to 2009, Biogeosciences, 15, 6713–6729, https://doi.org/10.5194/bg-15-6713-2018, 2018.

ESA: Copernicus Sentinel-2 (processed by ESA), 2021, MSI Level-2A BOA Reflectance Product. Collection 1., European Space Agency, https://doi.org/10.5270/S2_-znk9xsj, 2024.

Friedlingstein, P., O'Sullivan, M., Jones, M. W., Andrew, R. M., Bakker, D. C. E., Hauck, J., Landschützer, P., Le Quéré, C., Luijkx, I. T., Peters, G. P., Peters, W., Pongratz, J., Schwingshackl, C., Sitch, S., Canadell, J. G., Ciais, P., Jackson, R. B., Alin, S. R., Anthoni, P., Barbero, L., Bates, N. R., Becker, M., Bellouin, N., Decharme, B., Bopp, L., Brasika, I. B. M., Cadule, P., Chamberlain, M. A., Chandra, N., Chau, T.-T.-T., Chevallier, F., Chini, L. P., Cronin, M., Dou, X., Enyo, K., Evans, W., Falk, S., Feely, R. A., Feng, L., Ford, D. J., Gasser, T., Ghattas, J., Gkritzalis, T., Grassi, G., Gregor, L., Gruber, N., Gürses, O., Harris, I., Hefner, M., Heinke, J., Houghton, R. A., Hurtt, G. C., Iida, Y., Ilyina, T., Jacobson, A. R., Jain, A., Jarníková, T., Jersild, A., Jiang, F., Jin, Z., Joos, F., Kato, E., Keeling, R. F., Kennedy, D., Klein Goldewijk, K., Knauer, J., Korsbakken, J. I., Körtzinger, A., Lan, X., Lefèvre, N., Li, H., Liu, J., Liu, Z., Ma, L., Marland, G., Mayot, N., McGuire, P. C., McKinley, G. A., Meyer, G., Morgan, E. J., Munro, D. R., Nakaoka, S.-I., Niwa, Y., O'Brien, K. M., Olsen, A., Omar, A. M., Ono, T., Paulsen, M., Pierrot, D., Pocock, K., Poulter, B., Powis, C. M., Rehder, G., Resplandy, L., Robertson, E., Rödenbeck, C., Rosan, T. M., Schwinger, J., Séférian, R., Smallman, T. L., Smith, S. M., Sospedra-Alfonso, R., Sun, Q., Sutton, A. J., Sweeney, C., Takao, S., Tans, P. P., Tian, H., Tilbrook, B., Tsujino, H., Tubiello, F., van der Werf, G. R., van Ooijen, E., Wanninkhof, R., Watanabe, M., Wimart-Rousseau, C., Yang, D., Yang, X., Yuan, W., Yue, X., Zaehle, S., Zeng, J., and Zheng, B.: Global Carbon Budget 2023, Earth System Science Data, 15, 5301–5369, https://doi.org/10.5194/essd-15-5301-2023, 2023.

Gao, B.-C.: Normalized difference water index for remote sensing of vegetation liquid water from space, in: Imaging Spectrometry, edited by Descour, M. R., Mooney, J. M., Perry, D. L., and Illing, L. R., vol. 2480 of *Society of Photo-Optical Instrumentation Engineers (SPIE) Conference Series*, pp. 225–236, https://doi.org/10.1117/12.210877, 1995.

Gerbig, C.: Parameters for the Vegetation Photosynthesis and Respiration Model VPRM, https://doi.org/10.18160/HF4C-G0KK, 2024.

Gerbig, C. and Koch, F.-T.: Biosphere-atmosphere exchange fluxes for CO2 from the Vegetation Photosynthesis and Respiration Model VPRM for 2006-2021 (Version 1.0), https://doi.org/10.18160/VX78-HVA1, 2021.

Gerbig, C. and Koch, F.-T.: Biosphere-atmosphere exchange fluxes for CO2 from the Vegetation Photosynthesis and Respiration Model VPRM for 2022-2023, https://doi.org/10.18160/R5HS-YKW0, 2024.

Gourdji, S. M., Karion, A., Lopez-Coto, I., Ghosh, S., Mueller, K. L., Zhou, Y., Williams, C. A., Baker, I. T., Haynes, K. D., and Whetstone, J. R.: A Modified Vegetation Photosynthesis and Respiration Model (VPRM) for the Eastern USA and Canada, Evaluated With Comparison to Atmospheric Observations and Other Biospheric Models, Journal of Geophysical Research: Biogeosciences, 127, e2021JG006 290, https://doi.org/10.1029/2021JG006290, e2021JG006290 2021JG006290, 2022.

Hardiman, B. S., Wang, J. A., Hutyra, L. R., Gately, C. K., Getson, J. M., and Friedl, M. A.: Accounting for urban biogenic fluxes in regional carbon budgets, Science of The Total Environment, 592, 366–372, https://doi.org/10.1016/j.scitotenv.2017.03.028, 2017.

Hersbach, H., Bell, B., Berrisford, P., Hirahara, S., Horányi, A., Muñoz-Sabater, J., Nicolas, J., Peubey, C., Radu, R., Schepers, D., Simmons, A., Soci, C., Abdalla, S., Abellan, X., Balsamo, G., Bechtold, P., Biavati, G., Bidlot, J., Bonavita, M., De Chiara, G., Dahlgren, P., Dee, D., Diamantakis, M., Dragani, R., Flemming, J., Forbes, R., Fuentes, M., Geer, A., Haimberger, L., Healy, S., Hogan, R. J., Hólm, E., Janisková, M., Keeley, S., Laloyaux, P., Lopez, P., Lupu, C., Radnoti, G., de Rosnay, P., Rozum, I., Vamborg, F., Villaume, S., and Thépaut, J.-N.: The ERA5 global reanalysis, Quarterly Journal of the Royal Meteorological Society, 146, 1999–2049, https://doi.org/10.1002/qj.3803, 2020.

Hill, C., DeLuca, C., Balaji, Suarez, M., and Da Silva, A.: The architecture of the Earth System Modeling Framework, Computing in Science Engineering, 6, 18–28, https://doi.org/10.1109/MCISE.2004.1255817, 2004.

Huete, A., Didan, K., Miura, T., Rodriguez, E., Gao, X., and Ferreira, L.: Overview of the radiometric and biophysical performance of the MODIS vegetation indices, Remote Sensing of Environment, 83, 195–213, https://doi.org/10.1016/S0034-4257(02)00096-2, the Moderate Resolution Imaging Spectroradiometer (MODIS): a new generation of Land Surface Monitoring, 2002.

ICOS RI, Aalto, J., Aiguier, T., Alivernini, A., Aluome, C., Andersson, T., Arriga, N., Aurela, M., Back, J., Barten, S., Baur, T., Bazot, S., Beauclair, P., Becker, N., Becker, N., Belelli Marchesini, L., Bergström, G., Bernhofer, C., Berveiller, D., Biermann, T., Bloor, J., Bodson, B., Bogaerts, G., Bortoli, M., Bosio, I., Brut, A., Brümmer, C., Buchmann, N., Buysse, P., Båth, A., Calandrelli, D., Cavagna, M., Ceschia, E., Chabbi, A., Chebbi, W., Chianucci, F., Chipeaux, C., Chopin, H., Claverie, N., Cobbe, I., Colosse, D., Conte, A., Corsanici, R., Courtois, P., Coyle, M., Crill, P., Cuntz, M., Cuocolo, D., Czerný, R., DEPUYDT, J., Darenová, E., Darsonville, O., De Ligne, A., De Meulder, T., De Simon, G., Decau, M.-L., Dell'Acqua, A., Delorme, J.-P., Delpierre, N., Demoulin, L., Denou, J.-L., Di Matteo, B., Di Tommasi, P., Dienstbach, L., Dignam, R., Dolfus, D., Domec, J.-C., Douxfils, B., Dufrêne, E., Dumont, B., Durand, B., Eichelmann, U., Engelmann, T., Esposito, A., Esser, O., Etzold, S., Eugster, W., Famulari, D., Fares, S., Faurès, A., Feigenwinter, I., Feldmann, I., Fincham, W., Fischer, M., Foltýnová, L., Friborg, T., Galliot, J.-N., Garcia Quiros, I., Garrigou, C., Gasbarra, D., Gessler, A., Gharun, M., Gianelle, D., Gimper, S., Goded, I., Graf, A., Granouillac, F., Grenier, M., Grudd, H., Grünwald, T., Guillot, T., Harvey, D., Hatakka, J., Haustein, A., Hehn, M., Heinesch, B., Helfter, C., Heliasz, M., Holst, J., Holst, T., Hug, C., Häni, M., Hörtnagl, L., Ibrom, A., Ilardi, F., Jackowicz-Korczynski, M. A., Janssens, I., Jensen, R., Jocher, G., Joetzjer, E., Jones, M., Kempf, J., Kettler, M., Kljun, N., Klumpp, K., Kolari, P., Korrensalo, A., Kowalska, N., Kozii, N., Krejza, J., Kristoffersson, A., Kruijt, B., Kruszewski, A., Kumar, S., Kummer, S., Laakso, H., Lafont, S., Lange Rønn, E., Larmanou, E., Laurila, T., Leeson, S., Lefevre, L., Lehner, I., Lemaire, B., Levula, J., Levy, P., Liechti, K., Lily, J.-B., Limousin, J.-M., Linderson, M.-L., Lindgren, K., Lohila, A., Longdoz, B., Lootens, R., Loubet, B., Loustau, D., Lundin, E., López-Blanco, E., Löfvenius, P., Magliulo, V., Mammarella, I., Manco, A., Manise, T., Marcolla, B., Marek, M. V., Marklund, P., Marloie, O., Martin, R., Martin Saint Paul, N., Marty, M., Matilainen, T., Mattes, J., Matteucci, M., Mauder, M., Meier, P., Meire, A., Meis, J., Mensah, C., Michaud, L., Minerbi, S., Moderow, U., Montagnani, L., Moretti, V., Morfin, A., Mullinger, N., Mäkelä, T., Männikkö, M., Männistö, E., Mölder, M., Møller, F., Naiken, A., Naseer, M., Nemitz, E., Nezval, O., Nilsson, M., Orgun, A., Ottosson-Löfvenius, M., Ourcival, J.-M., Paasch, S., Pavelka, M., Peichl, M., Perot-Guillaume, C., Perrot, C., Pihlatie, M., Pilegaard, K., Piret, A., Prasse, H., Pumpanen, J., Rainne, J., Rakos, N., Rasmussen, L., Rebmann, C., Rinne, J., Rodeghiero, M., Roland, M., Rudd, D., Røjle Christensen, T., Schaarup Sørensen, J., Schmidt, M., Schmidt, P., Schmitt Oehler, M., Schrader, F., Segers, J., Simioni, G., Smith, P., Snellen, H., Sorgi, T., Soudani, K., Staník, K., Staudinger, M., Stecher, M., Stutz, T., Suopajärvi, S., Sutter, F., Taipale, R., Tallec, T., Tenca, F., Thimonier Rickenmann, A., Thyrion, T., Tomelleri, E., Tosca, M., Trotsiuk, V., Trusina, J., Tuittila, E.-S., Tuovinen, J.-P., Tyssandier, J., Tülp, H., Van Look, J., Varjonen, S., Vesala, T., Vescovo, L., Vincent, G., Vincke, C., Vitale, L., Vágner, L., Waldner, P., Wiesen, R., Winck, B., Yeung, K., Zampedri, R., Zawilski, B., Zenone, T., Zimmermann, S., Zweifel, R., van Dijk, N., van der Molen, M., Öquist, M., Šigut, L., Šlížek, J., and ICOS ETC: Ecosystem final quality (L2) product in ETC-Archive format - INTERIM release 2023-2, https://doi.org/10.18160/JYAR-7YEH, 2023.

Järvi, L., Nordbo, A., Junninen, H., Riikonen, A., Moilanen, J., Nikinmaa, E., and Vesala, T.: Seasonal and annual variation of carbon dioxide surface fluxes in Helsinki, Finland, in 2006–2010, Atmospheric Chemistry and Physics, 12, 8475–8489, https://doi.org/10.5194/acp-12-8475-2012, 2012.

Jiang, Z., Huete, A. R., Didan, K., and Miura, T.: Development of a two-band enhanced vegetation index without a blue band, Remote Sensing of Environment, 112, 3833–3845, https://doi.org/10.1016/j.rse.2008.06.006, 2008.

Jung, M., Henkel, K., Herold, M., and Churkina, G.: Exploiting synergies of global land cover products for carbon cycle modeling, Remote Sensing of Environment, 101, 534–553, https://doi.org/10.1016/j.rse.2006.01.020, 2006.

Kormann, R. and Meixner, F. X.: An analytical footprint model for non-neutral stratification, Boundary-Layer Meteorology, 99, 207–224, 2001.

Luus, K. A. and Lin, J. C.: The Polar Vegetation Photosynthesis and Respiration Model: a parsimonious, satellite-data-driven model of high-latitude CO_2 exchange, Geoscientific Model Development, 8, 2655–2674, https://doi.org/10.5194/gmd-8-2655-2015, 2015.

Mahadevan, P., Wofsy, S. C., Matross, D. M., Xiao, X., Dunn, A. L., Lin, J. C., Gerbig, C., Munger, J. W., Chow, V. Y., and Gottlieb, E. W.: A satellite-based biosphere parameterization for net ecosystem CO_2 exchange: Vegetation Photosynthesis and Respiration Model (VPRM), Global Biogeochemical Cycles, 22, https://doi.org/10.1029/2006GB002735, 2008.

https://doi.org/10.5194/egusphere-2024-3692
Preprint. Discussion started: 21 January 2025
© Author(s) 2025. CC BY 4.0 License.

Maksyutov, S., Eggleston, S., Woo, J. H., Fang, S., Witi, J., Gillenwater, M., Goodwin, J., and Tubiello, F.: Quality Assurance/Quality Control and Verification, 2019 Refinement to the 2006 IPCC Guidelines for National Greenhouse Gas Inventories, IPCC, https://www.ipcc-nggip.iges.or.jp/public/2019rf/pdf/1_Volume1/19R_V1_Ch06_QA_QC.pdf, accessed: 2024-09-14, 2019.

Matross, D. M., Arlyn Andrews, M. P., Gerbig, C., Lin, J. C., Wofsy, S. C., Daube, B. C., Gottlieb, E. W., Chow, V. Y., John T. Lee, C. Z., Bakwin, P. S., Munger, J. W., and Hollinger, D. Y.: Estimating regional carbon exchange in New England and Quebec by combining atmospheric, ground-based and satellite data, Tellus B: Chemical and Physical Meteorology, 58, 344–358, https://doi.org/10.1111/j.1600-0889.2006.00206.x, 2006.

Monteil, G., Broquet, G., Scholze, M., Lang, M., Karstens, U., Gerbig, C., Koch, F.-T., Smith, N. E., Thompson, R. L., Luijkx, I. T., White, E., Meesters, A., Ciais, P., Ganesan, A. L., Manning, A., Mischurow, M., Peters, W., Peylin, P., Tarniewicz, J., Rigby, M., Rödenbeck, C., Vermeulen, A., and Walton, E. M.: The regional European atmospheric transport inversion comparison, EUROCOM: first results on European-wide terrestrial carbon fluxes for the period 2006–2015, Atmospheric Chemistry and Physics, 20, 12 063–12 091, https://doi.org/10.5194/acp-20-12063-2020, 2020.

Moreno-Martínez, A., Izquierdo-Verdiguier, E., Maneta, M. P., Camps-Valls, G., Robinson, N., Muñoz-Marí, J., Sedano, F., Clinton, N., and Running, S. W.: Multispectral high resolution sensor fusion for smoothing and gap-filling in the cloud, Remote Sensing of Environment, 247, 111 901, https://doi.org/10.1016/j.rse.2020.111901, 2020.

Muñoz Sabater, J., Dutra, E., Agustí-Panareda, A., Albergel, C., Arduini, G., Balsamo, G., Boussetta, S., Choulga, M., Harrigan, S., Hersbach, H., Martens, B., Miralles, D. G., Piles, M., Rodríguez-Fernández, N. J., Zsoter, E., Buontempo, C., and Thépaut, J.-N.: ERA5-Land: a state-of-the-art global reanalysis dataset for land applications, Earth System Science Data, 13, 4349–4383, https://doi.org/10.5194/essd-13-4349-2021, 2021.

Munassar, S., Rödenbeck, C., Koch, F.-T., Totsche, K. U., Gałkowski, M., Walther, S., and Gerbig, C.: Net ecosystem exchange (NEE) estimates 2006–2019 over Europe from a pre-operational ensemble-inversion system, Atmospheric Chemistry and Physics, 22, 7875–7892, https://doi.org/10.5194/acp-22-7875-2022, 2022.

Niu, S., Chen, W., Liáng, L. L., Sierra, C. A., Xia, J., Wang, S., Heskel, M., Patel, K. F., Bond-Lamberty, B., Wang, J., et al.: Temperature responses of ecosystem respiration, Nature Reviews Earth & Environment, pp. 1–13, https://doi.org/10.1038/s43017-024-00569-3, 2024.

Pastorello, G., Trotta, C., Canfora, E., Chu, H., Christianson, D., Cheah, Y.-W., Poindexter, C., Chen, J., Elbashandy, A., Humphrey, M., Isaac, P., Polidori, D., Ribeca, A., van Ingen, C., Zhang, L., Amiro, B., and Ammann: The FLUXNET2015 dataset and the ONEFlux processing pipeline for eddy covariance data, Scientific Data, 7, 225, https://doi.org/10.1038/s41597-020-0534-3, 2020.

Peckham, S. E.: WRF/Chem version 3.3 user's guide, 2012.

Reichstein, M., Falge, E., Baldocchi, D., Papale, D., Aubinet, M., Berbigier, P., Bernhofer, C., Buchmann, N., Gilmanov, T., Granier, A., Grünwald, T., Havránková, K., Ilvesniemi, H., Janous, D., Knohl, A., Laurila, T., Lohila, A., Loustau, D., Matteucci, G., Meyers, T., Miglietta, F., Ourcival, J.-M., Pumpanen, J., Rambal, S., Rotenberg, E., Sanz, M., Tenhunen, J., Seufert, G., Vaccari, F., Vesala, T., Yakir, D., and Valentini, R.: On the separation of net ecosystem exchange into assimilation and ecosystem respiration: review and improved algorithm, Global Change Biology, 11, 1424–1439, https://doi.org/10.1111/j.1365-2486.2005.001002.x, 2005.

Roberts, C. D., Senan, R., Molteni, F., Boussetta, S., Mayer, M., and Keeley, S. P. E.: Climate model configurations of the ECMWF Integrated Forecasting System (ECMWF-IFS cycle 43r1) for HighResMIP, Geoscientific Model Development, 11, 3681–3712, https://doi.org/10.5194/gmd-11-3681-2018, 2018.

Rouse, J. W., Haas, R. H., Schell, J. A., Deering, D. W., et al.: Monitoring vegetation systems in the Great Plains with ERTS, NASA Spec. Publ, 351, 309, 1974.

© Author(s) 2025. CC BY 4.0 License.

Sargent, M., Barrera, Y., Nehrkorn, T., Hutyra, L. R., Gately, C. K., Jones, T., McKain, K., Sweeney, C., Hegarty, J., Hardiman, B., et al.: Anthropogenic and biogenic CO_2 fluxes in the Boston urban region, Proceedings of the National Academy of Sciences, 115, 7491–7496, https://doi.org/10.1073/pnas.1803715115, 2018.

Schmid, H.: Source areas for scalars and scalar fluxes, Boundary-Layer Meteorology, 67, 293–318, 1994.

Scholze, M., Kaminski, T., Knorr, W., Voßbeck, M., Wu, M., Ferrazzoli, P., Kerr, Y., Mialon, A., Richaume, P., Rodríguez-Fernández, N., Vittucci, C., Wigneron, J.-P., Mecklenburg, S., and Drusch, M.: Mean European Carbon Sink Over 2010–2015 Estimated by Simultaneous Assimilation of Atmospheric CO2, Soil Moisture, and Vegetation Optical Depth, Geophysical Research Letters, 46, 13 796–13 803, https://doi.org/https://doi.org/10.1029/2019GL085725, 2019.

Schröter, J., Rieger, D., Stassen, C., Vogel, H., Weimer, M., Werchner, S., Förstner, J., Prill, F., Reinert, D., Zängl, G., Giorgetta, M., Ruhnke, R., Vogel, B., and Braesicke, P.: ICON-ART 2.1: a flexible tracer framework and its application for composition studies in numerical weather forecasting and climate simulations, Geoscientific Model Development, 11, 4043–4068, https://doi.org/10.5194/gmd-11-4043-2018, 2018.

Souza, C. M., Z. Shimbo, J., Rosa, M. R., Parente, L. L., A. Alencar, A., Rudorff, B. F. T., Hasenack, H., Matsumoto, M., G. Ferreira, L., Souza-Filho, P. W. M., de Oliveira, S. W., Rocha, W. F., Fonseca, A. V., Marques, C. B., Diniz, C. G., Costa, D., Monteiro, D., Rosa, E. R., Vélez-Martin, E., Weber, E. J., Lenti, F. E. B., Paternost, F. F., Pareyn, F. G. C., Siqueira, J. V., Viera, J. L., Neto, L. C. F., Saraiva, M. M., Sales, M. H., Salgado, M. P. G., Vasconcelos, R., Galano, S., Mesquita, V. V., and Azevedo, T.: Reconstructing Three Decades of Land Use and Land Cover Changes in Brazilian Biomes with Landsat Archive and Earth Engine, Remote Sensing, 12, https://doi.org/10.3390/rs12172735, 2020.

Stocker, B. D., Zscheischler, J., Keenan, T. F., Prentice, I. C., Seneviratne, S. I., and Peñuelas, J.: Drought impacts on terrestrial primary production underestimated by satellite monitoring, Nature Geoscience, 12, 264–270, https://doi.org/10.1038/s41561-019-0318-6, 2019.

Sun, W., Luo, X., Fang, Y., Shiga, Y. P., Zhang, Y., Fisher, J. B., Keenan, T. F., and Michalak, A. M.: Biome-scale temperature sensitivity of ecosystem respiration revealed by atmospheric CO_2 observations, Nature Ecology & Evolution, 7, 1199–1210, https://doi.org/10.1038/s41559-023-02093-x, 2023.

Thompson, R. L., Broquet, G., Gerbig, C., Koch, T., Lang, M., Monteil, G., Munassar, S., Nickless, A., Scholze, M., Ramonet, M., et al.: Changes in net ecosystem exchange over Europe during the 2018 drought based on atmospheric observations, Philosophical Transactions of the Royal Society B, 375, 20190 512, 2020.

Vermote, E.: MODIS/Terra Surface Reflectance 8-Day L3 Global 500m SIN Grid V061, NASA EOSDIS Land Processes DAAC: Missoula, MT, USA, 2021.

Vermote, E., Franch, B., and Claverie, M.: VIIRS/NPP Surface Reflectance Daily L2G Global 1km and 500m SIN Grid V002 [Data set], ASA EOSDIS Land Processes Distributed Active Archive Center, https://doi.org/10.5067/VIIRS/VNP09GA.002, 2023.

Wutzler, T., Lucas-Moffat, A., Migliavacca, M., Knauer, J., Sickel, K., Šigut, L., Menzer, O., and Reichstein, M.: Basic and extensible post-processing of eddy covariance flux data with REddyProc, Biogeosciences, 15, 5015–5030, https://doi.org/10.5194/bg-15-5015-2018, 2018.

Zanaga, D., Van De Kerchove, R., Daems, D., De Keersmaecker, W., Brockmann, C., Kirches, G., Wevers, J., Cartus, O., Santoro, M., Fritz, S., Lesiv, M., Herold, M., Tsendbazar, N.-E., Xu, P., Ramoino, F., and Arino, O.: ESA WorldCover 10 m 2021 v200, https://doi.org/10.5281/zenodo.7254221, creative Commons Attribution 4.0 International, 2022.

https://doi.org/10.5194/egusphere-2024-3692
Preprint. Discussion started: 21 January 2025
© Author(s) 2025. CC BY 4.0 License.

Zhuang, J., raphael dussin, Huard, D., Bourgault, P., Banihirwe, A., Raynaud, S., Malevich, B., Schupfner, M., Filipe, Levang, S., Gauthier, C., Jüling, A., Almansi, M., RichardScottOZ, RondeauG, Rasp, S., Smith, T. J., Stachelek, J., Plough, M., Pierre, Bell, R., Caneill, R., and Li, X.: pangeo-data/xESMF: v0.8.2, https://doi.org/10.5281/zenodo.8356796, 2023.